Current-Starved Cross-Coupled CMOS Inverter Rings as Versatile Generators of Chaotic and Neural-Like Dynamics Over Multiple Frequency Decades

LUDOVICO MINATI[1,2,3], **(Senior Member, IEEE), MATTIA FRASCA**[4], **(Senior Member, IEEE),**
NATSUE YOSHIMURA[5,6], **LEONARDO RICCI**[7], **(Member, IEEE), PAWEŁ OŚWIĘCIMKA**[2],
YASUHARU KOIKE[5], **KAZUYA MASU**[8], **(Member, IEEE), AND HIROYUKI ITO**[5], **(Member, IEEE)**

[1]Tokyo Tech World Research Hub Initiative, Institute of Innovative Research, Tokyo Institute of Technology, Yokohama 226-8503, Japan
[2]Complex Systems Theory Department, Institute of Nuclear Physics, Polish Academy of Sciences, 31-342 Kraków, Poland
[3]Center for Mind/Brain Science, University of Trento, 38100 Trento, Italy
[4]Department of Electrical Electronic and Computer Engineering (DIEEI), University of Catania, 95125 Catania, Italy
[5]Laboratory for Future Interdisciplinary Research of Science and Technology (FIRST), Institute of Innovative Research, Tokyo Institute of Technology, Yokohama 226-8503, Japan
[6]PRESTO, JST, Saitama 332-0012, Japan
[7]Department of Physics and Center for Mind/Brain Science, University of Trento, 38100 Trento, Italy
[8]Tokyo Institute of Technology, Yokohama 226-8503, Japan

Corresponding author: Ludovico Minati (lminati@ieee.org)

ABSTRACT The generation of chaotic signals is relevant to a multitude of applications across telecommunications, random number generation, control, and the realization of distributed sensing systems; in addition, networks of coupled chaotic oscillators replicate diverse emergent phenomena occurring in considerably larger biological neural systems. However, to date, the generation of chaotic signals by means of complementary metal-oxide-silicon (CMOS) integrated circuits has been hampered largely by the need to implement reactive elements, and by limited flexibility. In this paper, we introduce a pure CMOS implementation of a chaos generator based on three inverter rings having lengths equal to the smallest odd prime numbers, i.e., 3, 5, and 7. These rings are cross-coupled via diodes of diverse strengths enabled through pass-gates, and the inverters in the rings are independently current-starved. Through numerical simulations and experiments, it is shown that this new topology can generate chaotic signals over at least four frequency decades. Furthermore, it is demonstrated that the experimental devices have access to a multitude of qualitatively-different dynamical behaviors as a function of the starving currents. In particular, the generation of spiking and bursting signals reminiscent of action potentials are observed, both with and without slower fluctuations which resemble field potentials. Furthermore, instances of oscillation quenching are found, wherein the circuit acts as a nonlinear amplifier yielding $1/f$-like stochastic signals. This compact and flexible topology promises to become a foundational cell in the design of integrated circuits requiring area-efficient, low-power, and controllable chaos generation.

INDEX TERMS Avalanching, CMOS inverter ring, chaotic oscillator, correlation dimension, current-starved, Kaplan-Yorke dimension, Lyapunov spectrum, neural-like signals, nonlinear oscillator, oscillation quenching, permutation entropy, signal generator, spectral flatness, spiking oscillator.

I. INTRODUCTION

The generation of chaotic signals via physical oscillators is of practical relevance to several fields encompassing secure

communication [1], encryption and random number generation [2], navigation and control applications in robotics [3], [4], as well as sonar and radar sensing [5], [6]. A developing application of chaotic oscillators is the realization of distributed networks of wirelessly-coupled nodes

The associate editor coordinating the review of this manuscript and approving it for publication was Woorham Bae.

L. Minati *et al.*: Current-Starved Cross-Coupled CMOS Inverter Rings as Versatile Generators of Chaotic and Neural-Like Dynamics

IEEE *Access*

realizing efficient sensing solutions based on notions of emergence and self-organization [7]–[9].

The chaotic oscillator implementations described in literature involve diverse nonlinearity sources, but are primarily based on discrete semiconductor components such as bipolar-junction transistors [10]–[13], or on operational amplifiers and analog multipliers [14], [15]. Monolithic bipolar and CMOS integrated-circuit implementations have also been proposed: early examples focused on Chua's circuit, considering inductor-less schemes [16] and equivalent state variables [17]; later, a Chua's circuit realization based on switched capacitors [18], a Lotka-Volterra prey-predator chaotic model [19], a circuit realizing an analog neural network [20], and one generating a multiscroll attractor [21] were reported. Further circuits tailored for random number generation have been introduced in [22], based on double-scroll-like attractors, and in [23], based on a cross-coupled LC architecture. Finally, discrete-time chaos generators were also designed [24], particularly to support the realization of logic elements [25]. Other studies have described multiscroll chaotic circuits based on floating-gate transistors [26], positive-type second-generation current conveyors [27], and the Lü chaotic oscillator [28]. Recent surveys of the design of integrated-circuit chaotic oscillators are found in [29] and [30].

The majority of these circuits involve one or more capacitors, polysilicon resistors or even inductors, and are therefore limited in their area efficiency, which in turn constrains their suitability for realizing single-chip networks of coupled oscillators. While elementary topologies such as rings can exhibit interesting properties, for instance, the spontaneous emergence of communities [31]–[33], neurally-inspired architectures suitable for implementing purposeful computation require large numbers of oscillators and complex connectivity [34], [35], which are problematic to realize unless the oscillator cells are highly area-efficient. Even though a systematic comparison is beyond the scope of this work, as a guideline we remark that, when realizing monolithic oscillator circuits requiring these elements, resistors, capacitors and inductors may take up more than half of the cell area, and for certain layouts even considerably more than that.

By exploiting the gate delay, the ring oscillator realizes the most compact type of CMOS oscillator circuit, as no additional components are required besides the inverter gates themselves. Notably, the intrinsic jitter in ring oscillators has already been used as an entropy source for random number generation [36], and stochastic variants have been realized by means of interposing inverters and multiplexers in order to alternate the induction of metastability and the generation of stable states [2]. In the context of ring oscillators, chaos generation was initially demonstrated in a configuration of two rings loaded with resistors and capacitors and coupled via diodes, thus not realizing a pure CMOS implementation [37]. More recently, however, a pure CMOS chaos generator was demonstrated, consisting of

inverter rings having lengths set to the smallest odd prime numbers, i.e., 3, 5 and 7, and cross-coupled using diodes: as no additional components are required, this configuration can potentially maximize the area efficiency. The underlying principle is that the absence of trivial ratios between prime numbers hinders the formation of stable phase relationships, as remarkably observed also biologically in the life cycles of certain insect species [38], [39], thus promoting the transition to chaos due to the attractive forces imparted by the couplings. In the initial implementation reported previously, a ring network was realized, and partial chaotic synchronization leading to the emergence of a community structure was documented [40].

A general limitation with the monolithic construction of chaotic oscillators is the reduced level of flexibility. This has hindered the acceptance of such circuits because it contrasts with the fact that, in many engineering and research applications, high versatility is needed as regards the frequency of the generated signals, their chaotic, periodic or quasi-periodic nature, and other qualitative features. In this paper, the previously-introduced oscillator based on cross-coupled inverter rings is generalized through the addition of current-starving circuitry: it is demonstrated that, crucially, this unlocks the generation of chaotic signals over a broad frequency range, including behaviors relevant to the study of neural-like dynamics. Firstly, the circuit design is introduced alongside simplified numerical models and associated results. Secondly, the physical implementation on a 0.18 μm technology node is presented. Thirdly, experimental results confirming the consistent generation of chaotic signals over multiple frequency decades are demonstrated. Fourthly, additional observations regarding the generation of neural-like signals in the form of spike trains, with and without field potential-like fluctuations and of stochastic signals under situations of oscillation quenching, are discussed. Finally, the possible applications of the proposed circuit architecture and steps for future research are considered.

II. CIRCUIT DESIGN AND SIMPLIFIED MODEL
A. THEORY AND ARCHITECTURE
The circuit consists of three inverter rings, having lengths equal to $n = 3$, 5 and 7 stages. To a first approximation, each inverter can be considered as an amplifier having a transconductance $\alpha < 0$ and charging a capacitor of value C, subject to a starving constraint of maximum source/sink current $I_s^{(n)}$, set to possibly different values between the three rings, and to a global constraint of limited output voltage swing within $\pm V_s$. Denoting v_a and v_q as the input and output voltages respectively (Fig. 1a), the output current of the inverter is a piece-wise linear function and can be written as

$$i(v_a, v_q) = S\Big(\alpha[R(v_a)H(V_s + v_q) - R(-v_a)H(V_s - v_q)], I_s^{(n)}\Big),$$

$$(1)$$

IEEE *Access*

L. Minati *et al.*: Current-Starved Cross-Coupled CMOS Inverter Rings as Versatile Generators of Chaotic and Neural-Like Dynamics
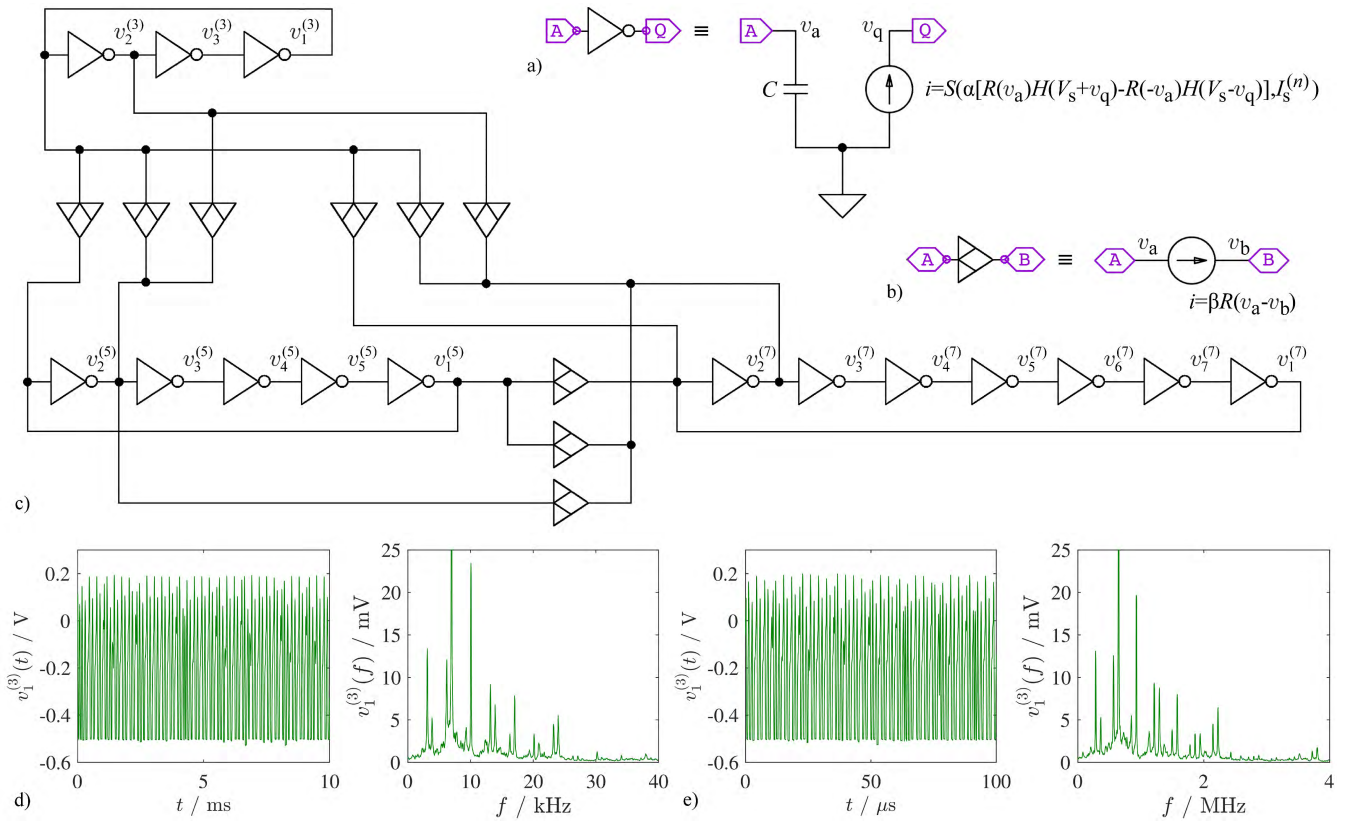
FIGURE 1. Chaotic oscillator circuit topology. a) Simplified model of the current-starved inverter cell containing the piece-wise nonlinearities $S(x, y)$, $H(x)$ and $R(x)$. b) Simplified model of the coupling cell with the piece-wise nonlinearity $R(x)$. c) Entire oscillator, wherein $v_j^{(n)}$ denotes the voltage at node j of the n-ring. d) Representative time-series and spectrum given $I_s = 1$ nA and $\beta = 1$ n℧. e) Representative time-series and spectrum given $I_s = 0.1$ μA and $\beta = 0.1$ μ℧. While not identical and despite the different scale, the temporal and spectral features appear closely overlapping. Ordinate axis scaled to magnify the lower peaks, truncating the highest one.

where a finite voltage swing is implemented via the Heaviside step function

$$H(x) = \begin{cases} 1 & \text{for } x > 0, \\ 0 & \text{otherwise} \end{cases} \quad (2)$$

and the ramp function

$$R(x) = xH(x); \quad (3)$$

here, bearing in mind that $\alpha < 0$, the terms $-\alpha R(-v_a)$ and $\alpha R(v_a)$ allow a positive and a negative output current, respectively, only when the output voltage is below positive saturation, i.e., $v_q < V_s$, and when it is above negative saturation, i.e., $v_q > -V_s$.

Current staving is similarly captured with

$$S(x, y) = \frac{x \min(|x|, y)}{|x|}. \quad (4)$$

Each ring is coupled to the one or two having a higher number of stages, i.e., $3 \leftrightarrow 5$, $3 \leftrightarrow 7$ and $5 \leftrightarrow 7$, via a coupling cell consisting of a nonlinear block resembling a diode. This can be approximated as a voltage-dependent current source instanced between the two nodes a and b (Fig. 1b), namely

another stage having a transconductance β, where

$$i(v_a, v_b) = \beta R(v_a - v_b). \quad (5)$$

The couplings are realized for two adjacent, arbitrarily-chosen nodes 1 and 2 in each ring, according to a scheme resembling cross-stitching with $1 \rightarrow 1$, $1 \rightarrow 2$ and $2 \rightarrow 2$; while several other arrangements can also provide chaoticity, this scheme was identified as the most effective one in the previous realization of the circuit, and was herein retained for consistency [40]. The resulting system equations can be written as shown in (6) at the top of the next page, where $v_j^{(n)}$ denotes the output voltage of the inverter stage j in the n-ring (Fig. 1c).

B. SIMULATIONS, TIME-SERIES ANALYSIS AND SYNCHRONIZATION

The chaotic dynamics of the coupled inverter rings are readily appreciable by simulating Eq. (6), as shown at the top of the next page, using the Adams-Bashforth-Moulton order 1-12 solver [41], setting $\alpha = -2.5$ μ℧ (1 ℧ = 1 S), $C = 40$ fF and $V_s = 0.5$ V, and operating the current-starving control parameters in unison across the three rings, i.e., with $I_s = I_s^{(3)} = I_s^{(5)} = I_s^{(7)}$. For instance, considering separately

L. Minati *et al.*: Current-Starved Cross-Coupled CMOS Inverter Rings as Versatile Generators of Chaotic and Neural-Like Dynamics

IEEE *Access*

$$
\begin{cases}
C\dfrac{dv_1^{(3)}}{dt} &= S(\alpha[R(v_3^{(3)})H(V_s + v_1^{(3)}) - R(-v_3^{(3)})H(V_s - v_1^{(3)})], I_s^{(3)}) \\
&\quad - \beta[R(v_1^{(3)} - v_1^{(5)}) + R(v_1^{(3)} - v_2^{(5)}) + R(v_1^{(3)} - v_1^{(7)}) + R(v_1^{(3)} - v_2^{(7)})] \\[4pt]
C\dfrac{dv_2^{(3)}}{dt} &= S(\alpha[R(v_1^{(3)})H(V_s + v_2^{(3)}) - R(-v_1^{(3)})H(V_s - v_2^{(3)})], I_s^{(3)}) \\
&\quad - \beta[R(v_2^{(3)} - v_2^{(5)}) + R(v_2^{(3)} - v_2^{(7)})] \\[4pt]
C\dfrac{dv_3^{(3)}}{dt} &= S(\alpha[R(v_2^{(3)})H(V_s + v_3^{(3)}) - R(-v_2^{(3)})H(V_s - v_3^{(3)})], I_s^{(3)}) \\[4pt]
C\dfrac{dv_1^{(5)}}{dt} &= S(\alpha[R(v_5^{(5)})H(V_s + v_1^{(5)}) - R(-v_5^{(5)})H(V_s - v_1^{(5)})], I_s^{(5)}) \\
&\quad + \beta[R(v_1^{(3)} - v_1^{(5)}) - R(v_1^{(5)} - v_1^{(7)}) - R(v_1^{(5)} - v_2^{(7)})] \\[4pt]
C\dfrac{dv_2^{(5)}}{dt} &= S(\alpha[R(v_1^{(5)})H(V_s + v_2^{(5)}) - R(-v_1^{(5)})H(V_s - v_2^{(5)})], I_s^{(5)}), \\
&\quad + \beta[R(v_1^{(3)} - v_2^{(5)}) + R(v_2^{(3)} - v_2^{(5)}) - R(v_2^{(5)} - v_2^{(7)})] \\
&\cdots \\
C\dfrac{dv_5^{(5)}}{dt} &= S(\alpha[R(v_4^{(5)})H(V_s + v_5^{(5)}) - R(-v_4^{(5)})H(V_s - v_5^{(5)})], I_s^{(5)}) \\[4pt]
C\dfrac{dv_1^{(7)}}{dt} &= S(\alpha[R(v_7^{(7)})H(V_s + v_1^{(7)}) - R(-v_7^{(7)})H(V_s - v_1^{(7)})], I_s^{(7)}) \\
&\quad + \beta[R(v_1^{(3)} - v_1^{(7)}) + R(v_1^{(5)} - v_1^{(7)})] \\[4pt]
C\dfrac{dv_2^{(7)}}{dt} &= S(\alpha[R(v_1^{(7)})H(V_s + v_2^{(7)}) - R(-v_1^{(7)})H(V_s - v_2^{(7)})], I_s^{(7)}) \\
&\quad + \beta[R(v_1^{(3)} - v_2^{(7)}) + R(v_2^{(3)} - v_2^{(7)}) + R(v_1^{(5)} - v_2^{(7)}) + R(v_2^{(5)} - v_2^{(7)})] \\
&\cdots \\
C\dfrac{dv_7^{(7)}}{dt} &= S(\alpha[R(v_6^{(7)})H(V_s + v_7^{(7)}) - R(-v_6^{(7)})H(V_s - v_7^{(7)})], I_s^{(7)})
\end{cases}
\tag{6}
$$

a lower-current, weaker-coupling case with $I_s = 1$ nA and $\beta = 1$ n℧ ($t_{end} = 0.1$ s, Fig. 1d) and a higher-current, stronger-coupling case with $I_s = 0.1$ μA and $\beta = 0.1$ μ℧ ($t_{end} = 1$ ms, Fig. 1e) revealed overlapping temporal and spectral features at two substantially different scales: calculating the centroid frequency [42] from the $i = 1 \ldots N$ binned spectral amplitudes x_i with

$$
f_\diamond = \frac{\sum_{i=1}^{N} f_i x_i}{\sum_{i=1}^{N} x_i}, \tag{7}
$$

the same was found to be, respectively, $f_\diamond \approx 19$ kHz and 1.7 MHz.

To evaluate their possible chaoticity, the corresponding time-series for $v_1^{(3)}$ were analyzed by means of time-delay embedding, setting the embedding lag to the first minimum of the time-lag mutual information function, the embedding dimension to the minimum integer number yielding $< 5\%$ of false nearest neighbors, and the Theiler window to the first maximum in the space-time separation plot [40], [43], [44]. The correlation dimension (D_2), which provides an estimate of the possibly fractional dimension of the underlying strange attractor, was estimated by means of the Grassberger-Procaccia method [45]. The largest Lyapunov exponent (λ_1), which determines the rate of exponential divergence, was estimated by means of the Kantz method [46]. For the two indicated I_s and β parameter settings and 20 runs with random initial conditions in $v(0) \in [0, 0.1]$, we obtained, respectively, $D_2 = 2.6 \pm 0.2$ and 2.1 ± 0.2 and $\lambda_1 = 0.02 \pm 0.003$ and 2.2 ± 0.3 μs^{-1} ($\mu \pm \sigma$); since within the given uncertainty levels one clearly has $\lambda_1 > 0$, this result confirms that, even in the context of a model based on stylized inverters and coupling cells, the proposed circuit topology could generate low-dimensional chaotic signals (conventionally intended as signals representing the projection of strange attractors having a fractal dimension smaller than 3) over a broad range of frequencies.

Additional insight into the circuit behavior could be obtained by considering the time-series at the individual nodes $v_j^{(n)}$. Chaoticity was primarily visible as fluctuations of the oscillation cycle amplitudes, particularly for the signals generated by the 3-ring: for $v_1^{(3)}$, the pattern was particularly asymmetric, with consistent negative saturation together with wide variability of the voltage corresponding to the unsaturated maximum in each cycle; for $v_2^{(3)}$, and even more so for $v_3^{(3)}$, the asymmetric pattern and cycle amplitude fluctuations were less prominent (Fig. 2a). Notably, an emergent property induced by the coupling scheme was a progressively more evident positive saturation over these three nodes. In the
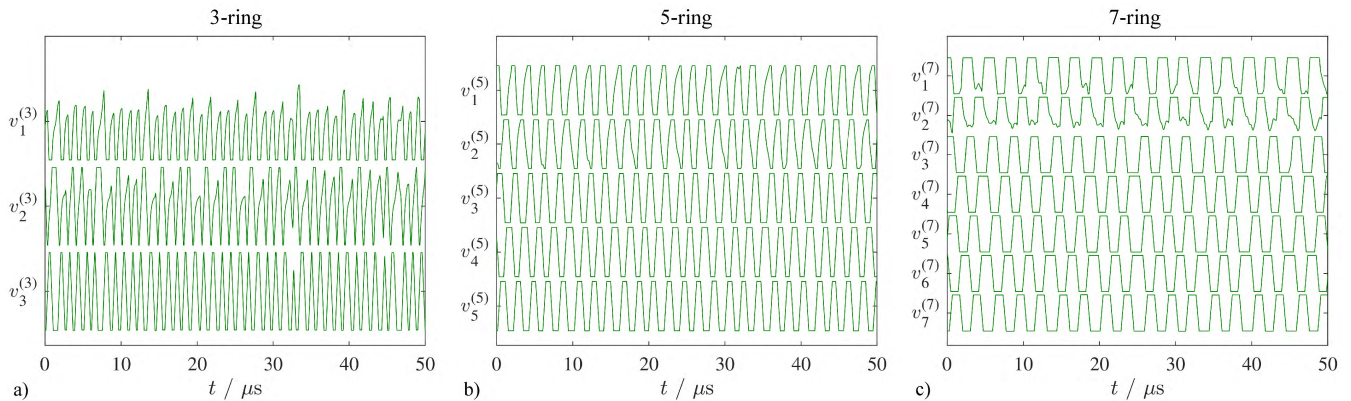
FIGURE 2. Time-series from all voltages $v_j^{(n)}$, for the inverter rings a) $n = 3$, b) $n = 5$ and c) $n = 7$, and nodes $j = 1 \ldots n$. Simulation assuming $I_s = 0.1 \ \mu A$ and $\beta = 0.1 \ \mu\mho$.

TABLE 1. Dynamical parameters for two representative settings of the parameters (starving current I_s and transconductance β) in the simplified numerical model (Eq. 6): Spectral flatness $\xi[v_j^{(n)}]$, intra-ring synchronization (across the inverters) $r[v_j^{(n)}, v_k^{(n)}]$ and inter-ring synchronization (across the coupling cells) $r[v_j^{(n)}, v_k^{(m)}]$. Values expressed as $\mu \pm \sigma$ over 20 runs with random initial conditions $v(0) \in [0, 0.1]$.

Spectral flatness	$I_s = 0.1 \ \mu A$ $\beta = 0.1 \ \mu\mho$	$I_s = 1 \ nA$ $\beta = 1 \ n\mho$	Intra-ring synchronization	$I_s = 0.1 \ \mu A$ $\beta = 0.1 \ \mu\mho$	$I_s = 1 \ nA$ $\beta = 1 \ n\mho$	Inter-ring synchronization	$I_s = 0.1 \ \mu A$ $\beta = 0.1 \ \mu\mho$	$I_s = 1 \ nA$ $\beta = 1 \ n\mho$
$\xi[v_1^{(3)}]$	0.31 ± 0.006	0.25 ± 0.003	$r[v_1^{(3)}, v_2^{(3)}]$	0.96 ± 0.0006	0.95 ± 0.0004	$r[v_1^{(3)}, v_1^{(5)}]$	0.22 ± 0.002	0.20 ± 0.002
$\xi[v_2^{(3)}]$	0.26 ± 0.007	0.23 ± 0.004	$r[v_2^{(3)}, v_3^{(3)}]$	0.95 ± 0.0004	0.95 ± 0.0003	$r[v_1^{(3)}, v_2^{(5)}]$	0.26 ± 0.002	0.23 ± 0.002
$\xi[v_3^{(3)}]$	0.19 ± 0.003	0.17 ± 0.001	$r[v_3^{(3)}, v_1^{(3)}]$	0.98 ± 0.0001	0.98 ± 0.0001	$r[v_2^{(3)}, v_2^{(5)}]$	0.28 ± 0.002	0.26 ± 0.001
$\xi[v_1^{(5)}]$	0.18 ± 0.009	0.15 ± 0.005	$r[v_1^{(5)}, v_2^{(5)}]$	0.98 ± 0.0001	0.98 ± 0.0001	$r[v_1^{(3)}, v_1^{(7)}]$	0.10 ± 0.002	0.08 ± 0.001
$\xi[v_2^{(5)}]$	0.19 ± 0.010	0.15 ± 0.003	$r[v_2^{(5)}, v_3^{(5)}]$	0.98 ± 0.0001	0.98 ± 0.0002	$r[v_1^{(3)}, v_2^{(7)}]$	0.12 ± 0.002	0.08 ± 0.001
$\xi[v_3^{(5)}]$	0.14 ± 0.005	0.12 ± 0.002	$r[v_3^{(5)}, v_4^{(5)}]$	0.99 ± 0.0000	0.99 ± 0.0001	$r[v_2^{(3)}, v_2^{(7)}]$	0.17 ± 0.001	0.15 ± 0.001
$\xi[v_4^{(5)}]$	0.14 ± 0.005	0.12 ± 0.003	$r[v_4^{(5)}, v_5^{(5)}]$	0.99 ± 0.0000	0.99 ± 0.0001			
$\xi[v_5^{(5)}]$	0.14 ± 0.004	0.13 ± 0.004	$r[v_5^{(5)}, v_1^{(5)}]$	0.99 ± 0.0001	0.99 ± 0.0001			
$\xi[v_1^{(7)}]$	0.19 ± 0.008	0.18 ± 0.004	$r[v_1^{(7)}, v_2^{(7)}]$	0.97 ± 0.0002	0.97 ± 0.0002	$r[v_1^{(5)}, v_1^{(7)}]$	0.17 ± 0.001	0.16 ± 0.002
$\xi[v_2^{(7)}]$	0.25 ± 0.008	0.21 ± 0.004	$r[v_2^{(7)}, v_3^{(7)}]$	0.97 ± 0.0002	0.97 ± 0.0002	$r[v_1^{(5)}, v_2^{(7)}]$	0.23 ± 0.002	0.21 ± 0.002
$\xi[v_3^{(7)}]$	0.13 ± 0.006	0.14 ± 0.003	$r[v_3^{(7)}, v_4^{(7)}]$	0.98 ± 0.0001	0.99 ± 0.0001	$r[v_2^{(5)}, v_2^{(7)}]$	0.24 ± 0.001	0.21 ± 0.002
$\xi[v_4^{(7)}]$	0.13 ± 0.004	0.14 ± 0.002	$r[v_4^{(7)}, v_5^{(7)}]$	0.98 ± 0.0001	0.99 ± 0.0001			
$\xi[v_5^{(7)}]$	0.13 ± 0.005	0.14 ± 0.002	$r[v_5^{(7)}, v_6^{(7)}]$	0.98 ± 0.0000	0.99 ± 0.0001			
$\xi[v_6^{(7)}]$	0.13 ± 0.005	0.14 ± 0.003	$r[v_6^{(7)}, v_7^{(7)}]$	0.98 ± 0.0001	0.99 ± 0.0001			
$\xi[v_7^{(7)}]$	0.13 ± 0.006	0.14 ± 0.002	$r[v_7^{(7)}, v_1^{(7)}]$	0.98 ± 0.0001	0.98 ± 0.0001			

5-ring and the 7-ring, chaoticity appeared more subtly and mainly in the form of irregular distortions of the trapezoid wave (Fig. 2b,c). Altogether, these results indicate that, even though all the three rings were necessary to engender the non-trivial frequency ratios, chaoticity was well-evident within the shortest one but relatively concealed by saturation in the other two. This observation was reflected in the values of spectral flatness (Table 1) [47], quantified as

$$\xi = \frac{N \left(\prod_{i=1}^{N} x_i \right)^{\frac{1}{N}}}{\sum_{i=1}^{N} x_i}, \qquad (8)$$

which, on average, was higher within the 3-ring ($\xi \approx 0.24$) than the 5,7-rings ($\xi \approx 0.15$), wherein the flatness was lowest for the non-coupled nodes ($\xi \approx 0.13$).

Further information on the dynamics could be extracted by considering the level of phase synchronization across each inverter and coupling cell. Towards this purpose, for each voltage time-series the corresponding analytic signal was obtained with

$$\psi_j^{(n)}(t) = v_j^{(n)}(t) + i\tilde{v}_j^{(n)}(t) = A_j^{(n)}(t)e^{i\varphi_j^{(n)}(t)}, \qquad (9)$$

where $i = \sqrt{-1}$ and $\tilde{v}_j^{(n)}(t)$ is the Hilbert transform of $v_j^{(n)}(t)$

$$\tilde{v}_j^{(n)}(t) = \frac{1}{\pi}\text{p.v.}\left[\int_{-\infty}^{\infty} \frac{v_j^{(n)}(\tau)}{t - \tau} d\tau \right], \qquad (10)$$

and where p.v. denotes the Cauchy principal value of the integral. From these, each instantaneous relative phase was derived as

$$\Delta\varphi(t) = \arg[\psi_j^{(n)}(t)\overline{\psi}_k^{(m)}(t)], \qquad (11)$$

yielding the phase-locking value [48]

$$r = |\langle e^{i\Delta\varphi(t)} \rangle_t|. \qquad (12)$$

As summarized in Table 1, on the one hand, phase synchronization across the inverters was near-complete, yet significantly lower than unity, particularly within the 3-ring,
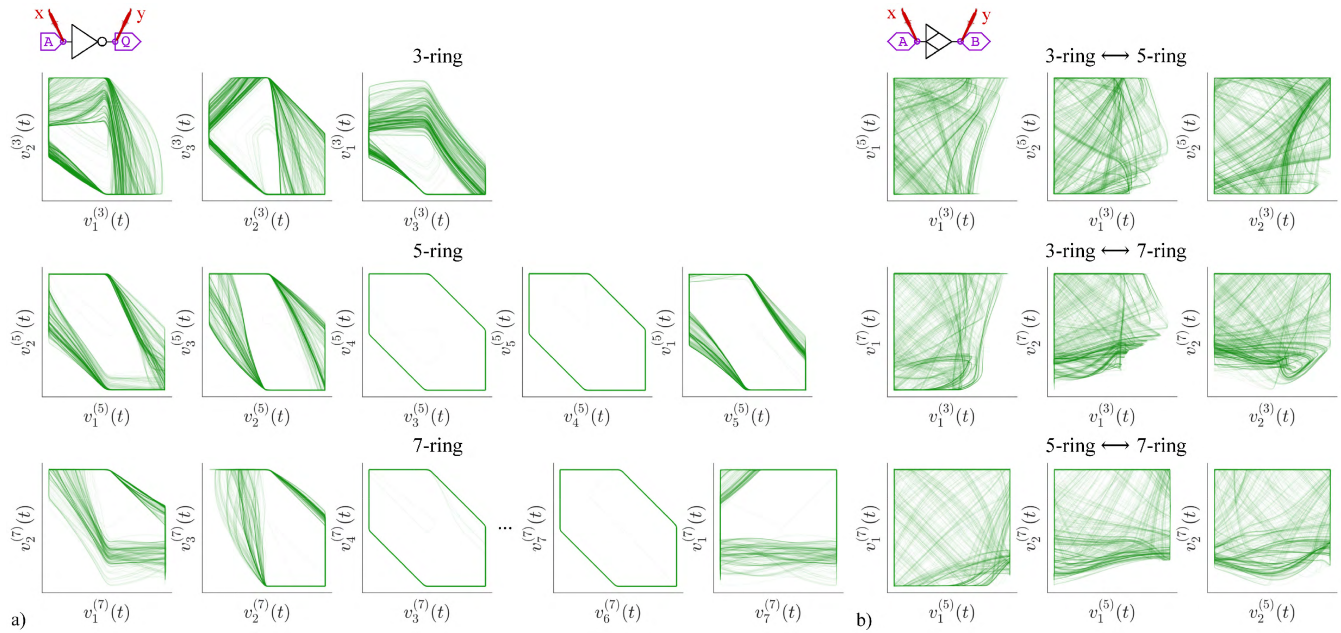
L. Minati *et al.*: Current-Starved Cross-Coupled CMOS Inverter Rings as Versatile Generators of Chaotic and Neural-Like Dynamics

IEEE *Access*

FIGURE 3. XY plots across a) the inverters and b) the coupling cells. Simulation assuming $I_s = 0.1\ \mu A$ and $\beta = 0.1\ \mu \mho$.

where $r \approx 0.96$ ($p < 0.001$); accordingly, the corresponding XY plots featured a chaotic trajectory, except for the inner, non-coupled nodes of the 5- and 7-rings, where a limit cycle-like orbit was apparent, due to the flattening effect of saturation (Fig. 3a). One the other hand, across the coupling cells, the phase synchronization parameter, albeit considerably lower, remained significantly greater than zero ($p < 0.001$), confirming the interactions between the rings supporting the maintenance of chaos. Its value depended on the differences in ring length, being on average stronger between the 3- and the 5-rings ($r \approx 0.24$), slightly weaker between the 5- and the 7-rings ($r \approx 0.20$) and about half the strength between the 3- and the 7-rings ($r \approx 0.12$). Accordingly, all XY plots across the coupled nodes featured clearly chaotic trajectories (Fig. 3b). Albeit with some differences, the observed features were consistent over the wide frequency range considered.

C. REVISED MODEL AND LYAPUNOV EXPONENT SPECTRUM

While formally parsimonious, the simplified model considered thus far is not realistic in that it contains discontinuities. A more physically-plausible system, differentiable everywhere, can be obtained by replacing the Heaviside function with a hyperbolic tangent, i.e.,

$$H(x) = \frac{1 + \tanh (x/x_t)}{2}, \tag{13}$$

where $x_t = 10$ mV, and representing current starving as

$$S(x, y) = y \tanh(kx/y), \tag{14}$$

where $k = 2.5$; the precise settings of x_t and k are not critical. The qualitative features of the dynamics are essentially unal-

tered, confirming the robustness of chaos generation (data not shown). The model thus written is well-suited for integration using the explicit embedded Runge-Kutta Prince-Dormand order-$(8, 9)$ method and concomitant application of the so-called standard method, which provides a robust manner of directly determining the entire spectrum of Lyapunov exponents of a flow given its Jacobian matrix [49]–[53]. To this end, the state variables were recorded every $dt = 1.6$ ns, which is more than an order of magnitude smaller than the characteristic time-scale of the system's evolution. The Gram-Schmidt orthogonalization required by the standard method was performed every 10-1,000 steps.

Based on the sorted Lyapunov exponents $\lambda_i \geq \lambda_{i+1}$, the Kaplan-Yorke (or Lyapunov) dimension D_{KY} was obtained with

$$D_{KY} = k + \sum_{i=1}^{k} \frac{\lambda_i}{|\lambda_{k+1}|}, \tag{15}$$

where k is the largest integer for which the sum of the k largest exponents is non-negative [54]. Considering, without loss of generality, the case $I_s = 1\ \mu A$ and $\beta = 1\ \mu \mho$, we obtained a single positive Lyapunov exponent, namely $\lambda_1 = 0.8 \pm 0.1\ \mu s^{-1}$, and a dimension $D_{KY} = 2.4 \pm 0.1$. The different magnitude of λ_1 compared to the previous section should principally be ascribed to the different parameter settings and to the different representation of the nonlinearities, i.e. Eq. (13) vs. Eq. (2), and Eq. (14) vs. (4). This result provides a more definite confirmation of chaoticity, compared to the application of methods based on scalar time-series such as those employed above, which may be problematic as regards distinguishing chaoticity and quasi-periodicity.

IEEE *Access*

L. Minati *et al.*: Current-Starved Cross-Coupled CMOS Inverter Rings as Versatile Generators of Chaotic and Neural-Like Dynamics

III. EXPERIMENTAL REALIZATION

A. CIRCUIT IMPLEMENTATION

The experimental prototypes were realized on a 0.18 μm, 6-metal, 1-poly technology node with RF option (Taiwan Semiconductor Manufacturing Co. Ltd., Hsinchu). The current-starved inverters were constructed according to the dimensions indicated in Fig. 4a, without any additional load capacitance beyond that inherent in the MOS gates and routing lines (tentatively estimated at 40 fF). Incidentally, for all practical purposes, at the oscillation frequencies considered in the present study, the effect of parasitic routing resistances and inductances could be neglected. Notably, in the context of sensing applications, capacitive elements may be connected at the inverter nodes to influence the dynamics based on the physical variable(s) of interest.

The maximum source and sink currents were jointly set via the voltages V_{BPn} and V_{BNn}, which were controlled independently for the $n = 3, 5$ and 7 rings, setting $V_{BNn} = V_{Bn}$ where V_{Bn} is an externally-applied control potential, and generating V_{BPn} via the input branch of the current mirror, having dimensions 3μm/1μm and 1μm/1μm, shown in Fig. 4b. Again in the context of sensing applications, these potentials may reflect external environmental inputs, as well as be used to tune oscillation towards a frequency range desirable for efficient wireless communication [7]–[9]. The coupling cells were obtained by realizing a diode via a pair of two counterposed PMOS/NMOS transistors of respective widths $3w$ and w, as shown in Fig. 4c. By means of pass-gates, four banks having $w = 0.25, 0.5, 1$ and 2 μm could be connected in parallel, effectively yielding a 4-bit digital-to-analog converter for the coupling strengths (parameter β). The coupling cells linking the 3-ring to the 5-ring, and those linking the 3-ring and 5-ring to the 7-ring, were in principle controllable separately but here operated in unison. To minimize the circuit complexity, a single output buffer [55] was implemented as visible in Fig. 4d, extracting only the signal corresponding to $v_1^{(3)}$ as indicated in Fig. 4e. In the future, a radio-frequency transmitter and/or receiver amplifier could be connected to this node for implementing wireless couplings.

B. SPICE SIMULATIONS

To verify the viability of the proposed implementation, simulations were performed using the `LTspice XVII` environment (Analog Devices, Inc., Norwood MA, USA), based on the freely-available 180 nm bulk CMOS technology-predictive models [56], which yielded results in agreement with the fab proprietary design kits (data not shown). The entire circuit in Fig. 4e was simulated, including the current-starved inverter in Fig. 4a, the current-mirror in Fig. 4b and the coupling cell in Fig. 4c, but excluding the output buffer in Fig. 4d and saving directly the time-series for $v_1^{(3)}$.

The supply voltage was set to $V_C = 1$ V, the width of the coupling cell to $w = 0.25$ μm, the control voltages were swept in unison, with $V_{B3} = V_{B5} = V_{B7} = V_B$ and 80 equispaced runs in $V_B = 0.2$-0.6 V, and the simulation time was adaptively set based on the oscillation frequency, between $t_{end} = 50$ μs-0.2 s.

Sustained oscillation was observed over the entire range $f_\diamond \approx 5$ kHz-20 MHz. In particular, chaotic signals with $D_2 \approx 1.5$-2.9 and $\xi \approx 0.3$-0.5 were consistently generated beyond ≈ 1 MHz (Fig. 5a); below this frequency, chaotic operation could also be attained, but, depending on the coupling width, chaotic and periodic bands coexisted (data not shown). In agreement with the simplified model, asymmetric signals with qualitatively similar features were observed across the ranges of ≈ 1 kHz (Fig. 5b), ≈ 100 kHz (Fig. 5c), ≈ 1 MHz (Fig. 5d) and ≈ 10 MHz (Fig. 5e). Notably, mainly as a consequence of the realistic transistor model, involving a more complex nonlinearity, here the control voltage did not have the effect of merely shifting the frequency spectrum, but also considerably affected its qualitative features: this is in contrast with the simulations based on the simplified model shown in Fig. 1d,e and was, at least in part, related to a more convoluted effect the couplings. At the same time, anticipating some of the experimental results detailed below, a certain level of heterogeneity was noticeable as regards the variance and the patterns of cycle amplitude fluctuation.

C. TESTBED AND DATA ACQUISITION

The circuit layout is presented in Fig. 6a alongside the corresponding die microphotograph in Fig. 6b. The overall area in this preliminary implementation, dubbed `CHARM-2` was $\approx 28,000$ μm^2, however, it could, in principle, be straightforwardly reduced down to $< 10,000$ μm^2 by fixing the coupling strengths. The present implementation was preliminary in nature and aimed at confirming feasibility while maximizing flexibility, without yet attempting to optimize density or minimize parasitics. The device-under-test (DUT), in the form of a die shared between multiple projects, was directly bonded to a low-loss laminate circuit board, shown in Fig. 6c, containing all supporting circuitry, and provided via U.FL connectors for the output signals together with a header connector for power supply and control connections. Five device specimens, thereafter referred to as units $u = 1 \ldots 5$, were fabricated and used in the experimental measurements.

As indicated in Fig. 4e, the output buffer was biased with a low-inductance resistor having $R = 470$ Ω, yielding a parasitic board-level RC filter having $f_c \approx 170$ MHz, clearly adequate for the present purposes. The signal was buffered by a wide-band, low-bias amplifier (LTC6268; Analog Devices, Inc.) and digitized using a digital-storage oscilloscope type WaveJet 354T (LeCroy Inc., Chestnut Ridge NY, USA) for 5 million points, with a sampling rate adjusted between 25 kSa/s and 2 GSa/s depending on the oscillation frequency, and a resolution enhancement up to 12 bit. The experimental signals are freely downloadable [57].

The data acquisition process was automated under the control of a MatLab script (MathWorks Inc., Natick MA, USA) and an Arduino Mega microcontroller (Arduino, Ivrea, Italy), in turn interfaced via I2C bus to a digital IO buffer (PCA9534;
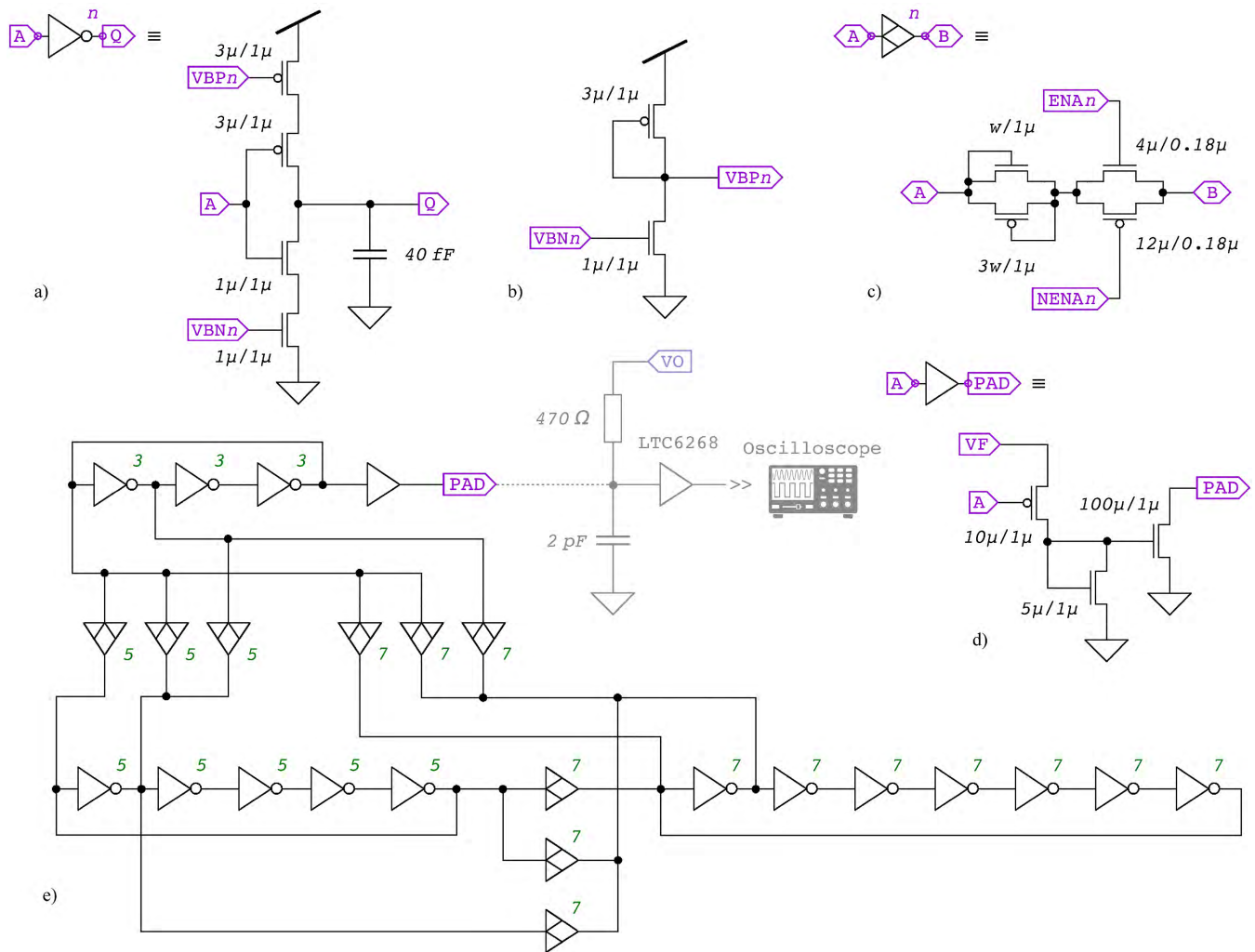
L. Minati *et al.*: Current-Starved Cross-Coupled CMOS Inverter Rings as Versatile Generators of Chaotic and Neural-Like Dynamics

IEEE *Access*

FIGURE 4. Chaotic oscillator circuit design. a) Current-starved inverter cell (supply voltage: V_C). The signals V_{BPn}/V_{BNn} are differently connected to the voltages V_{BP3}/V_{BN3}, V_{BP5}/V_{BN5} and V_{BP7}/V_{BN7} (not shown) for the inverters in the 3-, 5- and 7-rings, respectively. The 40 fF capacitor represents the gate and parasitic (e.g., routing) capacitances. b) Input branch of the current mirror. c) Coupling cell, consisting of a dual NMOS/PMOS diode in series to a pass gate. The signals $ENA_n/NENA_n$ are connected to the digital lines $ENA_5/NENA_5$ and $ENA_7/NENA_7$ (not shown) for enabling/disabling the couplings of the 5- and 7-rings, respectively. In the physical device, four independently-controlled cells were paralleled, having gate widths $w = 0.25, 0.5, 1$ and 2 μm and providing discrete control over the parameter β. d) Open-drain output buffer cell (supply voltage: V_F). e) Entire oscillator, including the board-level pull-up resistor to the voltage V_O and output buffer amplifier; the 2 pF capacitor represents the board-level node capacitance (including the amplifier's input).

NXP Inc., Eindhoven, The Netherlands) for controlling the aggregate width w of the enabled coupling cells, and 8-bit digital-to-analog converters (AD5305; Analog Devices, Inc.) generating the control voltages including V_{B3}, V_{B5} and V_{B7}. The core voltage was always set to $V_C = 1$ V and the supply voltage to the external resistor was always set to $V_O = 0.6$ V. To minimize distortion, the supply voltage for the output buffer was controlled dynamically, aiming for $\approx 50\%$ duty-cycle at each frequency while setting $w = 0$ (no coupling, periodic square wave oscillation), yielding $V_F = 1.5\text{-}1.6$ V. To estimate power dissipation by the core cell, the current on the voltage rail V_C was monitored by a current-sensing amplifier (MAX9938; Maxim Inc., San Jose CA, USA).

D. CHAOTICITY AT A TUNABLE FREQUENCY
To study the behavior of the experimental devices, the current in the 3-ring was taken as the primary control parameter,

and the generated signals were evaluated over the voltage range $V_{B3} = 0.2\text{-}0.75$ V. In contrast with the SPICE simulations, instead of fixing $V_{B3} = V_{B5} = V_{B7}$, here the effects of V_{B5} and V_{B7} were explored independently, alongside that of the coupling strength w. While a noticeable heterogeneity between the five realized specimens was present due to manufacturing tolerances, overall the generated signals had reproducible features. The dynamical parameters for eight representative combinations of the control voltage settings are reported in Table 2, separately for two chosen devices to demonstrate the reproducibility. Generation of chaotic dynamics was reliably observed over the frequency range $f_\diamond \approx 2$ kHz-15 MHz, with a relatively stable amplitude $v_{RMS} \approx 0.1\text{-}0.2$ V. Even slower oscillation could be obtained, but less consistently (data not shown); on the other hand, increasing the control voltage beyond this range did not elevate the frequency further, because the same was
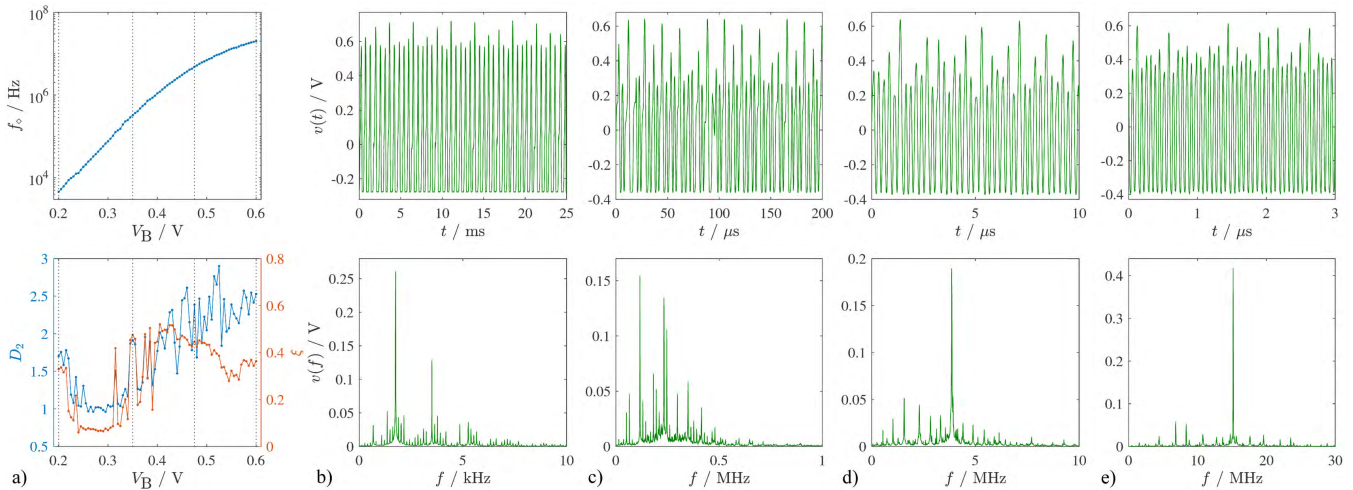
IEEE *Access*

L. Minati *et al.*: Current-Starved Cross-Coupled CMOS Inverter Rings as Versatile Generators of Chaotic and Neural-Like Dynamics

FIGURE 5. SPICE simulations assuming core supply voltage $V_C = 1$ V and control voltages $V_{B3} = V_{B5} = V_{B7} = V_B$. The voltage $v(t)$ represents the input to the output buffer (Fig. 4d), not included in these simulations. a) Spectral centroid $f_\diamond$ (top), correlation dimension D_2 and spectral flatness ξ (bottom) as a function of V_B. The dashed lines denote the voltages chosen for visualization of representative time-series (top) and spectra (bottom), namely: b) $V_B = 0.2$ V, c) $V_B = 0.35$ V, d) $V_B = 0.48$ V and e) $V_B = 0.6$ V.

TABLE 2. Experimentally-measured dynamical parameters for representative settings (control voltages V_{B3}, V_{B5} and V_{B7} and selected diode width w) over two physical devices u: Core power dissipation P_C, root-mean-square output voltage amplitude v_{RMS}, spectral centroid $f_\diamond$, spectral flatness ξ, nonlinear decorrelation time τ, correlation dimension D_2 and its uncertainty δD_2, order 5 permutation entropy on local extrema amplitudes $h_5^{(E)}$. Averages over 10 surrogates denoted with $\hat{D}_2$, $\delta\hat{D}_2$ and $\hat{h}_5^{(E)}$; superscript $(*)$, $(**)$ and $(***)$ respectively denote $p < 0.05$, $p < 0.01$ and $p < 0.001$ for comparison with the experimental data.

V_{B3}/V	V_{B5}/V	V_{B7}/V	w/μm	P_C/μW	u	v_{RMS}/V	$f_\diamond$/MHz	ξ	τ / μs	D_2 ($\hat{D}_2$)	δD_2 ($\delta\hat{D}_2$)	$h_5^{(E)}$ ($\hat{h}_5^{(E)}$)
0.24	0.16	0.24	0.25	0.05	1	0.16	0.002	0.44	196.00	1.78 (4.59)$^{(***)}$	0.63 (5.65)$^{(***)}$	0.48 (0.70)$^{(***)}$
					3	0.15	0.002	0.42	267.60	1.61 (4.69)$^{(***)}$	0.54 (5.43)$^{(***)}$	0.49 (0.70)$^{(***)}$
0.31	0.24	0.30	0.25	0.1	2	0.13	0.011	0.42	41.80	1.93 (4.92)$^{(***)}$	0.31 (5.06)$^{(***)}$	0.41 (0.70)$^{(***)}$
					3	0.16	0.014	0.44	36.00	2.17 (4.74)$^{(***)}$	0.34 (4.98)$^{(***)}$	0.40 (0.67)$^{(***)}$
0.30	0.30	0.35	0.25	0.2	2	0.11	0.025	0.37	20.24	2.49 (5.22)$^{(***)}$	0.58 (5.79)$^{(***)}$	0.54 (0.71)$^{(***)}$
					4	0.11	0.039	0.35	25.36	2.14 (6.94)$^{(***)}$	0.49 (7.82)$^{(***)}$	0.54 (0.72)$^{(***)}$
0.36	0.31	0.35	0.25	0.2	2	0.12	0.056	0.36	8.47	2.04 (4.19)$^{(***)}$	0.45 (4.56)$^{(***)}$	0.46 (0.69)$^{(***)}$
					3	0.12	0.068	0.35	7.67	2.34 (4.16)$^{(***)}$	0.45 (4.42)$^{(***)}$	0.51 (0.69)$^{(***)}$
0.38	0.34	0.43	0.25	0.7	3	0.09	0.221	0.28	2.42	2.49 (4.75)$^{(***)}$	0.35 (5.76)$^{(***)}$	0.62 (0.70)$^{(***)}$
					4	0.09	0.369	0.35	1.35	2.42 (5.27)$^{(***)}$	0.55 (6.49)$^{(***)}$	0.57 (0.69)$^{(***)}$
0.47	0.47	0.46	0.25	2.0	1	0.12	2.486	0.33	0.26	2.52 (4.97)$^{(***)}$	0.36 (5.64)$^{(***)}$	0.53 (0.70)$^{(***)}$
					4	0.11	2.650	0.34	0.22	2.42 (5.68)$^{(***)}$	0.44 (6.89)$^{(***)}$	0.48 (0.71)$^{(***)}$
0.60	0.61	0.61	2.00	12.3	1	0.16	9.124	0.55	0.05	2.64 (4.23)$^{(***)}$	0.56 (5.42)$^{(***)}$	0.59 (0.70)$^{(***)}$
					2	0.14	7.400	0.59	0.06	2.60 (5.17)$^{(***)}$	0.44 (6.11)$^{(***)}$	0.59 (0.70)$^{(***)}$
0.71	0.73	0.73	2.00	25.0	1	0.17	16.729	0.45	0.03	2.66 (3.62)$^{(*)}$	0.71 (4.41)$^{(***)}$	0.50 (0.67)$^{(***)}$
					3	0.16	15.025	0.43	0.03	2.38 (3.93)$^{(***)}$	0.56 (4.71)$^{(***)}$	0.55 (0.66)$^{(***)}$

inherently limited by the current-carrying capability of the inverter MOS pairs. The coupling strength (diode channel width) at which chaoticity was most consistently observed was $w = 0.25$ μm below 5 MHz, and $w = 2$ μm above it. By comparison, the previous realization of the oscillator, implemented on a 0.7 μm process and devoid of current-starving circuitry, generated spectra centered around a fixed frequency of $\approx$ 4 MHz [40]. The core power dissipation varied by almost three orders of magnitude, being estimated at < 100 nW at the lowest setting, plausibly dominated by leakage effects, and peaking at 25 μW for the highest frequency; the overall low power dissipation renders this circuit of interest for realizing nodes powered using energy harvesting or super-capacitor approaches.

The spectral flatness tended to be higher at the edges of the frequency range under consideration, with $\xi \approx$ 0.3-0.6. Notably, this parameter tended to be more elevated than observed at the same circuit node in the simplified numerical model and SPICE simulations, suggesting, as expected, that the greater complexity of the nonlinearities and the heterogeneities in the physical system supported the generation of richer signals. The spectral centroid is a linear measure, and the characteristic time-scale of the dynamics is more appropriately represented by the delay τ corresponding to the first local minimum of the time-lag normalized mutual information $I_x(\delta t)/H_x$, where $I_x(\delta t)$ denotes the mutual information at delay δt and H_x the Shannon entropy [58]. Also according to this parameter, which is sensitive to nonlinear

L. Minati *et al.*: Current-Starved Cross-Coupled CMOS Inverter Rings as Versatile Generators of Chaotic and Neural-Like Dynamics
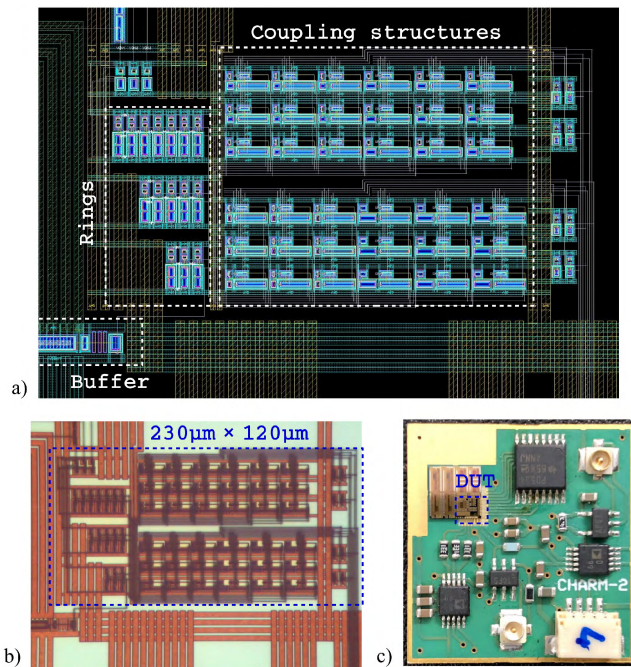
IEEE Access

FIGURE 6. Physical realization. a) CMOS layout design, b) Die microphotograph and c) Characterization circuit board with bonded die (top-left corner).

correlations, there was a span of approximately four orders of magnitude, namely $\tau \approx 30$ ns-200 μs.

In line with the SPICE simulations, the correlation dimension tended to grow with frequency, indicating an increasing geometrical complexity of the underlying strange attractor over the range $D_2 \approx 1.6$-2.7, with a relatively narrow corresponding estimation uncertainty $\delta D_2 \approx 0.3$-0.6, which confirmed the adequate temporal self-similarity of the dynamics [43], [45]. This range overlapped the results from the previous realization of this circuit topology without current-starving [40], as well as typical observations from oscillators based on one or two discrete transistors [13], [59], and various other chaotic electronic circuits [60]. To corroborate the validity of these estimates, 10 surrogate time-series were generated for each measurement, randomly shuffling the phases while retaining the frequency amplitudes as well as the value distribution [61]: their correlation sum slope curves did not converge, and the corresponding values of D_2 and δD_2 were considerably higher, with $p < 0.001$ in all cases.

For the experimental data, estimation of the Lyapunov exponents was avoided due to its possibly greater sensitivity to noise and discretization efforts [44], [46]. Instead, further indication of the chaotic dynamics was obtained by calculating the permutation entropy, which is a robust measure of complexity based on the relative frequencies of the possible symbol-sequence patterns, defined on the basis of the relative ranks of samples $x_i, x_{i+\tau} \dots x_{i+(m-1)\tau}$ in a time-series $X = \{x_i\}$ for $i = 1, \dots, N$ [62]. For this purpose, the experimental time-series were converted from a flow-like to a map-like representation by extracting the local extrema (subsequent minima and maxima, $\tau = 1$) with an estimator based

on the first and second derivatives, and the embedding order was set to $m = 5$. The resulting values were in the range of $h_5^{(E)} \approx 0.4$-0.6, namely, intermediate between the lower levels $h \approx 0$-0.4 expected for periodic or quasi-periodic signals and the higher ones $h \approx 0.8$-1 commonly denoting noise-like fluctuations [63]; accordingly, they were significantly below the estimates calculated on the surrogate time-series, with $p < 0.001$ in all cases (importantly, to avoid bias, the signals were shuffled before determining the extrema).

E. DIVERSITY OF DYNAMICS

Four representative experimental time-series, alongside the corresponding spectra and time-lag reconstructions of the attractors (wherein insight into the qualitative features of dynamics is obtained through plotting a time-series versus a copy of itself delayed according to a suitably-chosen lag), are visible in Fig. 7. On the whole, the signals had qualitative features in agreement with the simulations involving the simplified numerical model and the SPICE model, and with the previous realization devoid of current-starving circuitry [40]: chaoticity was primarily evident in the form of irregular cycle amplitudes, particularly as regards the maxima. Upon closer inspection, however, some differences between them could be noticed. First, while the frequency content was generally characterized by a predominant broad distribution with overlapping discrete peaks, for operation at the lower frequencies the baseline became flatter and the discrete peaks more clearly distinguishable, suggesting less irregular dynamics (e.g., Fig. 7a vs. c). Accordingly, the orbits as reconstructed via time-delay embedding delineated an attractor of changing morphology: at the lowest frequencies, it had the appearance of nested loops expected in the presence of distinguishable frequency components (Fig. 7a). Then, it morphed towards a shape intermediate between that generated by the chaotic Colpitts oscillator and that of a spiking process (Fig. 7c), and eventually arrived at a dumpling-like appearance (Fig. 7d) [60], [64], [65]. The spectral features and attractor morphology were evidently similar in each chosen pair of device specimens.

Further useful insight into the time-domain features could be obtained via considering some additional parameters. First, denoting the time-series of maxima amplitudes as $X^{(\max)}$, the unitary-lag correlation was calculated, yielding for the four cases shown $r[x_i^{(\max)}, x_{i+1}^{(\max)}] = -0.9, -0.5, -0.2$ and -0.4, respectively. This indicated that the dynamics were, albeit to a diverse extent, always anti-persistent, which may signal the presence of underlying period-doubling bifurcation [64]: the route-to-chaos mechanism of this system requires elucidation in future work. Second, the amplitude variance asymmetry was $\log(\sigma^2[X^{(\max)}]/\sigma^2[X^{(\min)}]) = 0.3, 0.8, 4.4$ and 3.0: in other words, the variance was always greater for the maxima than for the minima, more markedly so for the higher oscillation frequency settings, in line with the simulations and the previous realization of the oscillator [40]. A positive value
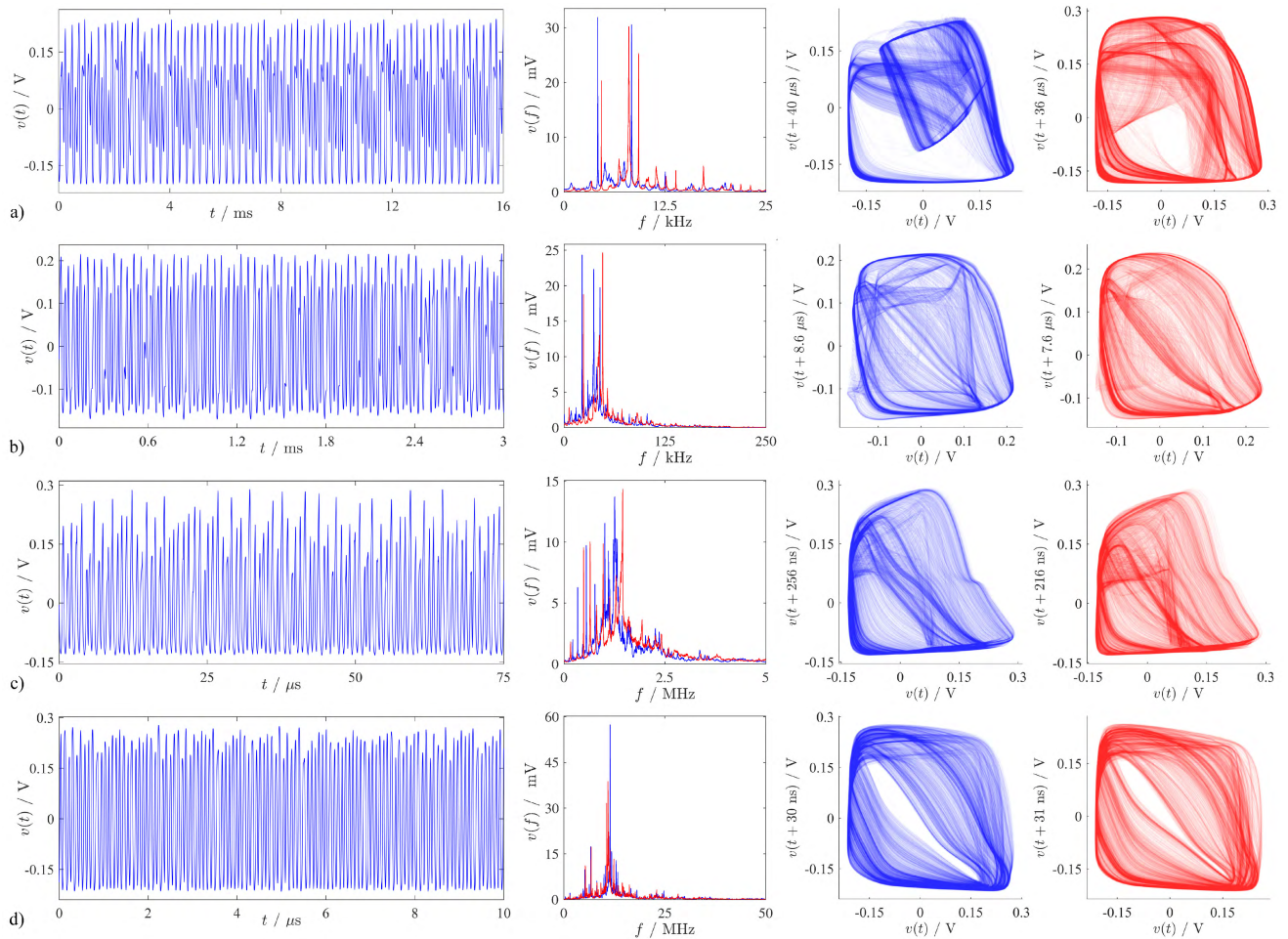
FIGURE 7. Representative examples of oscillation dynamics measured experimentally at different settings, and their reproducibility across two realizations. Left to right: Time-series, frequency spectrum, time-lag embedded attractors (lag equal to the first minimum of the time-lag mutual information function). Blue/right: different physical circuit specimens u. a) $V_C = 1$ V, $V_F = 1.58$ V, $V_O = 0.6$ V, $V_{B3} = 0.31$ V, $V_{B5} = 0.24$ V, $V_{B7} = 0.30$ V, $w = 0.25$ μm, blue: $u = 2$, red: $u = 3$; b) $V_C = 1$ V, $V_F = 1.58$ V, $V_O = 0.6$V, $V_{B3} = 0.36$ V, $V_{B5} = 0.31$ V, $V_{B7} = 0.35$ V, $w = 0.25$ μm, blue: $u = 2$, red: $u = 3$; c) $V_C = 1$ V, $V_F = 1.58$ V, $V_O = 0.6$ V, $V_{B3} = 0.47$ V, $V_{B5} = 0.47$ V, $V_{B7} = 0.46$ V, $w = 0.25$ μm, blue: $u = 1$, red: $u = 4$; d) $V_C = 1$ V, $V_F = 1.48$ V, $V_O = 0.6$ V, $V_{B3} = 0.71$ V, $V_{B5} = 0.73$ V, $V_{B7} = 0.73$ V, $w = 2$ μm, blue: $u = 1$, red: $u = 3$. Sample rate: 1 MSa/s in a), 10 MSa/s in b), 250 MSa/s in c), and 2 GSa/s in d).

for this parameter, originally introduced in neurophysiology as a putative proxy of criticality, denotes a propensity of the system variable to return to a lower value, akin to the action of a gravitational field [66]. Because the PMOS and NMOS arms of the inverter rings were dimensioned to be approximately symmetric (ratio 3:1, Fig. 4a), and the corresponding equations in the simplified numerical model were by definition symmetric around zero, this result highlights an emergent property of the dynamics, possibly related to the connection topology of the cross-coupling diodes (reversing their polarities, however, did not have the straightforward effect of inverting the asymmetry). Third, even though irregular amplitude fluctuations are the most visually compelling feature of these signals, as also observed for many other electronic chaotic oscillators [13], [60], one should more rigorously quantify separately the coefficients of variation for the maxima amplitudes and cycle periods, namely $\sigma[X^{(max)}]/\mu[X^{(max)}]$ and $\sigma[X^{(\Delta t)}]/\mu[X^{(\Delta t)}]$. Aside from the high variation due to strong anti-persistence

in Fig. 7a, different features were evident for the remaining three signals. For the case in Fig. 7b, due to the presence of brief "pauses" yielding the signal a burst-like appearance, in relative terms the variation was actually slightly higher for the periods than the amplitudes, with $\sigma[X^{(\Delta t)}]/\mu[X^{(\Delta t)}] \approx 0.31$ and $\sigma[X^{(max)}]/\mu[X^{(max)}] \approx 0.24$. The converse was true for Fig. 7c, with $\sigma[X^{(\Delta t)}]/\mu[X^{(\Delta t)}] \approx 0.20$ and $\sigma[X^{(max)}]/\mu[X^{(max)}] \approx 0.3$, whereas for Fig. 7d, the situation was balanced, with $\sigma[X^{(\Delta t)}]/\mu[X^{(\Delta t)}] \approx 0.11$ and $\sigma[X^{(max)}]/\mu[X^{(max)}] \approx 0.11$.

To further illustrate the diversity of the emergent dynamics, additional examples are provided in Fig. 8 (one in the ≈ 1 MHz range, and two in the ≈ 10 kHz range) and the corresponding dynamical parameters are given in Table 3. These behaviors depended on the individual device tolerances and thus were not observed for the same control parameter settings across the realized devices. First, a situation resembling that in Fig. 7c is presented, however with an attractor more closely resembling a spike-like geometry, whose
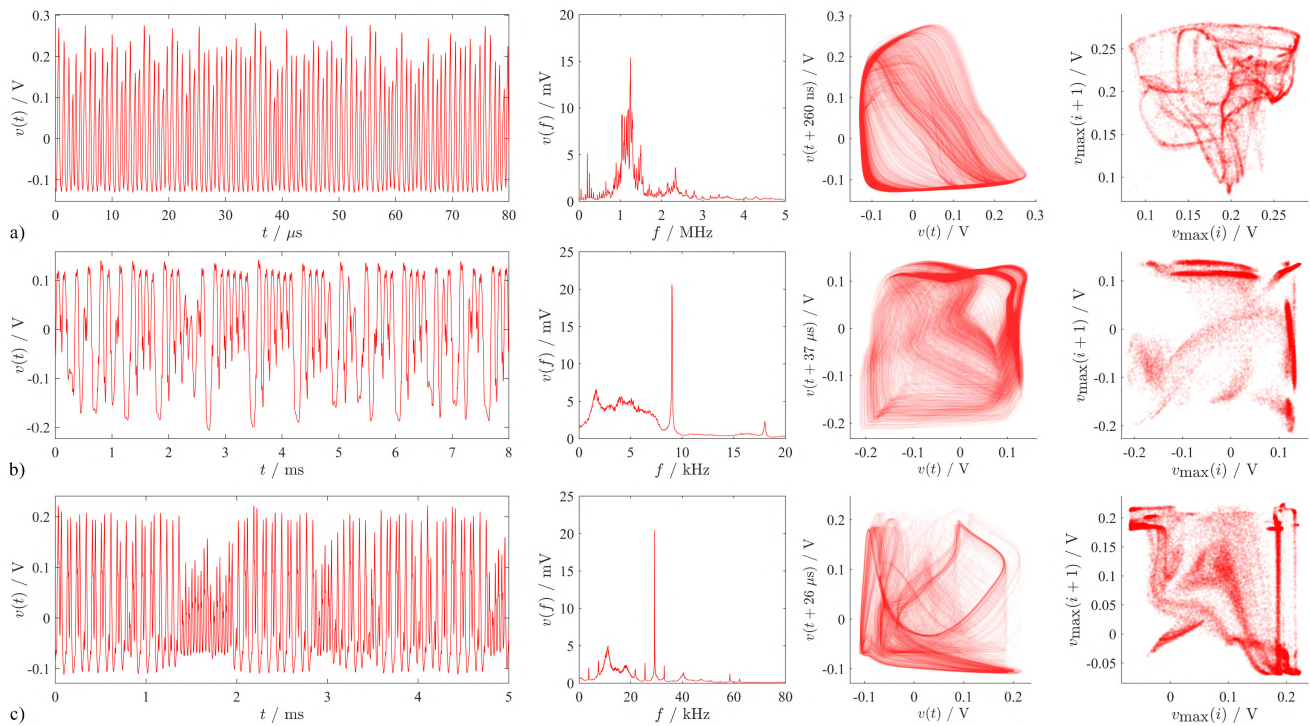
L. Minati et al.: Current-Starved Cross-Coupled CMOS Inverter Rings as Versatile Generators of Chaotic and Neural-Like Dynamics

IEEE Access

FIGURE 8. Examples of the diversity of emergent dynamics. Left to right: Time-series, frequency spectrum, time-lag embedded attractor (lag equal to the first minimum of the time-lag mutual information function), Poincaré section (amplitudes of successive local maxima). a) Higher-dimensional chaos, $V_C = 1$ V, $V_F = 1.58$ V, $V_O = 0.6$ V, $V_{B3} = 0.47$ V, $V_{B5} = 0.44$ V, $V_{B7} = 0.43$ V, $w = 0.5$ μm, $u = 1$; b) Generation of irregular volleys, yielding a cardioid-shaped attractor, $V_C = 1$ V, $V_F = 1.58$ V, $V_O = 0.60$ V, $V_{B3} = 0.28$ V, $V_{B5} = 0.30$ V, $V_{B7} = 0.33$ V, $w = 0.25$ μm, $u = 2$; c) Unstable alternation of high-amplitude, low-frequency and lower-amplitude, higher-frequency oscillations, $V_C = 1$ V, $V_F = 1.58$ V, $V_O = 0.60$ V, $V_{B3} = 0.31$ V, $V_{B5} = 0.36$ V, $V_{B7} = 0.31$ V, $w = 0.25$ μm, $u = 3$. Sample rate: 250 MSa/s in a), 2.5 MSa/s in b) and c).

underlying complexity could be more properly appreciated on the corresponding Poincaré section for local maxima (an arbitrarily chosen plane sectioning an attractor in two and thereby enabling visualization of its complex geometry beyond what is possible by time-lag embedding of the continuous trajectory), which revealed a highly-folded structure; this translated into the highest observed correlation dimension, $D_2 = 2.9$, approaching the threshold $D > 3$ commonly considered as indicative of high-dimensional chaos (Fig. 8a) [64]. Second, a behavior involving the generation of "volleys" of large cycles, irregular in their amplitudes, number, and separation, is presented. In this case, which resembled behaviors observed at the mesoscale for neural systems [67] and results for some discrete transistor-based oscillators [60], [68], the spectrum exhibited a single, narrow peak together with a broad distribution of activity at lower frequencies; the corresponding attractor was cardioid-shaped, and the Poincaré section revealed that the points were mainly clustered onto three ellipsoidal clouds (Fig. 8b). Third, an instance of intermittency is shown, wherein segments of large-amplitude but slower oscillations alternated with segments of weaker but faster activity, representing a behavior also occurring in nonlinear pendula [69] and plasmas [70]. While the frequency spectrum was reminiscent of the previous case, the underlying attractor was considerably more complicated, as expected given that it represents the overlap of multiple regimes (Fig. 8c). In future

work, intermittency effects will be evaluated as means of relaying information across spatially-extended networks wherein significant couplings are limited to neighboring nodes [7]–[9], [64].

Summing up, the detailed experimental results presented in this and the previous section confirm the physical viability of the proposed oscillator circuit, and the ability of its present realization to generate chaotic dynamics over at least four frequency decades. Even though no optimization for reducing the impact of the device tolerances was performed, the main features of the signals were overall satisfactorily reproducible, with additional anecdotal evidence of further, qualitatively-different behaviors which are pervasive in other physical systems [64] and electronic oscillators [60] but not observable in the previous realization of this oscillator due to its limited flexibility. Not only the signals reproduced many features found in discrete transistor-based oscillators requiring large reactive components, but the results also demonstrated considerable versatility in that the control parameters could be straightforwardly changed by means of voltage and digital signals.

IV. ADDITIONAL OBSERVATIONS
A. NEURAL-LIKE DYNAMICS
Unlike the signals described thus far, in biological neural recordings the amplitude of action potentials (spikes) is effectively binarized, and irregularity is manifest in the

TABLE 3. Experimentally-measured dynamical parameters for examples of diverse dynamics, including avalanching and oscillation quenching, given control voltages V_{B3}, V_{B5} and V_{B7}, and selected diode width w in a chosen physical device u: Root-mean-square output voltage amplitude v_{RMS} (in the absence of core supply voltage, i.e., $V_C = 0$ V, v'_{RMS}), spectral centroid $f_\diamond$, spectral flatness ξ, nonlinear decorrelation time τ, correlation dimension D_2 and its uncertainty δD_2. The order-5 permutation entropy was calculated on local extrema amplitudes for $h_5^{(E)}$, inter-event intervals for $h_5^{(\Delta t)}$ and with time-lag embedding for $h_5^{(\tau)}$. Averages over 10 surrogates are denoted with $\hat{D}_2$, $\delta\hat{D}_2$ and $\hat{h}_5$; superscript (*), (**) and (* * *) respectively denote $p < 0.05$, $p < 0.01$ and $p < 0.001$ for comparison with the experimental data.

V_{B3} / V	V_{B5} / V	V_{B7} / V	w / μm	u	v_{RMS} / V	$f_\diamond$ / MHz	ξ	τ / μs	D_2 ($\hat{D}_2$)	δD_2 ($\delta\hat{D}_2$)	$h_5^{(E)}$ ($\hat{h}_5^{(E)}$)
						Examples of the diversity of emergent dynamics (Fig. 8)					
0.47	0.44	0.43	0.50	1	0.12	2.388	0.36	0.27	2.93 (4.22)$^{(***)}$	0.54 (5.82)$^{(***)}$	0.54 (0.68)$^{(***)}$
0.28	0.30	0.33	0.25	2	0.10	0.014	0.31	37.16	2.38 (5.29)$^{(***)}$	0.63 (5.11)$^{(***)}$	0.50 (0.66)$^{(***)}$
0.31	0.36	0.31	0.25	3	0.09	0.036	0.40	26.48	2.32 (5.72)$^{(***)}$	0.56 (6.81)$^{(***)}$	0.61 (0.72)$^{(***)}$
V_{B3} / V	V_{B5} / V	V_{B7} / V	w / μm	u	v_{RMS} / V	$f_\diamond$ / kHz	ξ	τ / ms	D_2 ($\hat{D}_2$)	δD_2 ($\delta\hat{D}_2$)	$h_5^{(\Delta t)}$ ($\hat{h}_5^{(\Delta t)}$)
						Examples of the generation of spike-like signals (Fig. 9)					
0.24	0.25	0.25	0.75	1	0.12	1.980	0.40	0.25	0.88 (4.39)$^{(***)}$	1.12 (5.16)$^{(***)}$	0.94 (0.98)$^{(***)}$
0.16	0.14	0.12	0.25	4	0.14	0.151	0.43	6.52	2.39 (4.96)$^{(***)}$	1.86 (5.11)$^{(***)}$	0.73 (0.98)$^{(***)}$
0.16	0.19	0.23	0.50	5	0.12	0.356	0.52	1.68	4.07 (4.30)	2.42 (9.25)$^{(***)}$	0.87 (1.00)$^{(***)}$
V_{B3} / V	V_{B5} / V	V_{B7} / V	w / μm	u	v_{RMS} (v'_{RMS}) / mV	$f_\diamond$ / kHz	ξ	τ / ms	D_2 ($\hat{D}_2$)	δD_2 ($\delta\hat{D}_2$)	$h_5^{(\tau)}$ ($\hat{h}_5^{(\tau)}$)
						Examples of oscillation quenching situations (Fig. 11)					
0.21	0.21	0.20	0.25	1	2.73 (0.05)	1.246	0.37	3.72	5.58 (7.09)	11.21 (11.31)	1.00 (1.00)$^{(***)}$
0.14	0.04	0.10	0.25	2	2.02 (0.05)	0.728	0.26	10.89	7.00 (6.81)	10.59 (10.45)	0.97 (0.97)
0.12	0.10	0.08	0.25	4	1.73 (0.03)	0.678	0.25	11.98	5.33 (4.38)	7.85 (9.39)	0.98 (0.98)

inter-spike intervals. Far from being a system-specific feature, the generation of spiking dynamics, possibly accompanied by signatures of criticality, has been observed as an emergent property across widely diverse nonlinear physical systems, especially in relation to integrate-and-fire-like processes [59], [71]. In particular, a multitude of electronic circuits have been devised which produce irregular trains of spikes and bursts, mostly involving realistic CMOS-based implementations of neural equations wherein voltages and currents have clear associations to physiological magnitudes [35]. Similar behaviors have also been elicited in a considerably smaller circuit based on two discrete bipolar-junction transistors [13], as well as in a lattice network containing gas-discharge tubes as the only nonlinear elements [72].

Here, experimental evidence is presented which exemplifies the ability of the proposed circuit to also yield, for suitable settings of the control parameters, spiking dynamics qualitatively reminiscent of several aspects in neurophysiological recordings. For brevity, no attempts are made to rigorously derive the conditions under which this behavior is generated, but the fact that it was never apparent in extensive simulations of the simplified model (data not shown) suggests that parametric heterogeneities and perhaps also the complex response characteristics of the physical MOS transistors may play an important role [59]. Three instances of spiking with different statistical features are reported, for different parameter setting combinations that depended on the individual tolerances of the realized devices, and led to activity in the 100-1,000 Hz range.

The time-series and associated analyses are shown in Fig. 9, alongside the corresponding dynamical parameters in Table 3. The case in Fig. 9a is characterized by almost completely quantized spike amplitudes, involving the generation of trains (avalanches) containing approximately evenly-spaced events interspersed with pauses. As previously

documented for the two transistor-based spiking oscillator, a behavior of this kind could be underlined by oscillation with a strong periodic component, involving a closed orbit with a finite bifurcation probability, according to which the trajectory may enter a larger orbit corresponding to the spike generation [13]. Given suitable thresholds for spike detection and the segmentation of avalanches, namely amplitude $\hat{v} = 0.15$ V and inter-spike interval $\widehat{\Delta t} = \langle \Delta t \rangle$, the histogram of the avalanche sizes $p(s)$, where s is the number of spikes in an avalanche, could be obtained: for critical neural dynamics and other critical branching processes, the distribution diverges and a power-law decay with slope $\alpha = -3/2$ is consistently observed [73]. Here, however, for $s < 10$ there was clearly no evidence of power-law scaling, on the contrary there were even large and irregular deviations with respect to the shuffled surrogates. Nevertheless, for $s > 10$ the distribution was more regular and appeared somewhat more heavy-tailed compared to the exponential decay of the surrogates. We, therefore, calculated the Fano factor binning the point process in windows having widths $T = 10^{-2}$-10^{3} ms according to

$$F(T) = \frac{\sigma_T^2}{\mu_T}, \qquad (16)$$

where σ_T^2 and μ_T denote the variance and mean of the binned event counts. Over the range $T = 10^{0}$-10^{3} ms, the distribution became clearly separate from the surrogates and over-dispersed, and power-law scaling with a slope of $\delta = 0.23$ was established. This result is a possible indicator of criticality, and a similar relationship is found both in biological spike-trains and in the previously-mentioned gas-discharge tube-based model of critical dynamics, albeit with larger $\delta \approx 0.5$-0.8 [72], [74]. Although this finding should be interpreted cautiously, the Fano factor and the avalanche distribution analyses knowingly involve different assumptions, hence, particularly given the quantization of inter-spike intervals (see below), it is possible that the evidence of
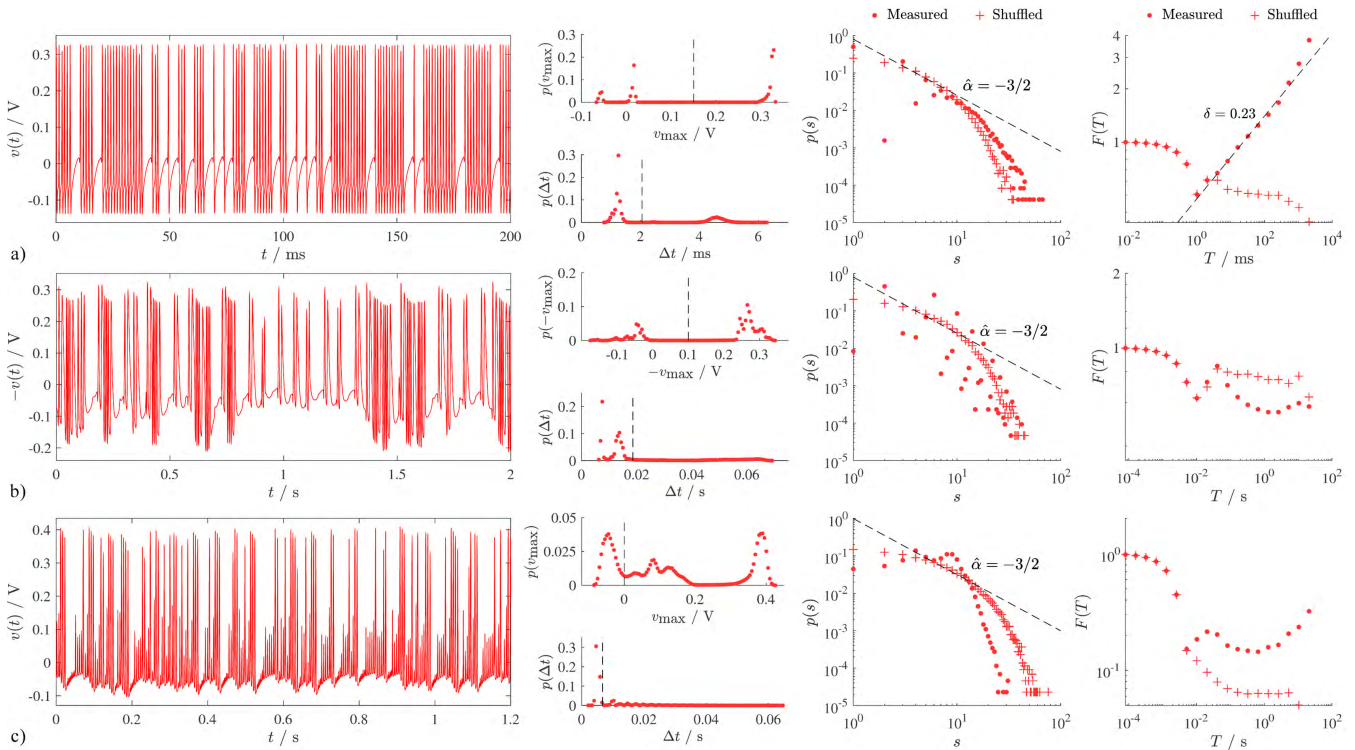
L. Minati *et al.*: Current-Starved Cross-Coupled CMOS Inverter Rings as Versatile Generators of Chaotic and Neural-Like Dynamics

IEEE *Access*

FIGURE 9. Examples of the generation of spike-like signals. Left to right: Time-series, amplitude histogram $p(v_{max})$ with spike detection threshold (top) and inter-spike interval histogram $p(\Delta t)$ with threshold for avalanche detection (bottom), distribution of avalanche size $p(s)$ (predetermined power-law with $\hat{\alpha} = -3/2$ shown for comparison), Fano factor as a function of window size $F(T)$ (slope δ fit where scaling evident). a) $V_C = 1$ V, $V_F = 1.59$ V, $V_O = 0.6$ V, $V_{B3} = 0.24$ V, $V_{B5} = 0.25$ V, $V_{B7} = 0.25$ V, $w = 0.75$ μm, $u = 1$; b) $V_C = 1$ V, $V_F = 1.62$ V, $V_O = 0.60$ V, $V_{B3} = 0.16$ V, $V_{B5} = 0.14$ V, $V_{B7} = 0.12$ V, $w = 0.25$ μm, $u = 4$; c) $V_C = 1$ V, $V_F = 1.62$ V, $V_O = 0.60$ V, $V_{B3} = 0.16$ V, $V_{B5} = 0.19$ V, $V_{B7} = 0.23$ V, $w = 0.5$ μm, $u = 5$. Sample rate: 250 kSa/s in a), 25 kSa/s in b) and c).

scale-free activity was too weak to be detected by both analyses [71].

On the other hand, the time-series in Fig. 9b and Fig. 9c feature spikes having prominent amplitude variation, additionally in the context of a baseline exhibiting slow and large fluctuations; in these cases, there was no power-law scaling, and the spike distribution was always under-dispersed.

In neurophysiological signals such as single-cell recordings, two components of activity are commonly distinguished: action potentials, hallmarked by rapid fluctuations having large and quantized amplitude, and local field potentials, characterized by smaller, and slower, continuous fluctuations. These index, respectively, the pre- and post-synaptic activity, in that the former represent the neuron's output and the latter result from spatiotemporal summation within the dendritic trees. Given the qualitative differences between Fig. 9a and Fig. 9b, it appears worthwhile to reconsider the signals from this perspective. Towards that purpose, the same were split into low- and high-frequency components by means of second-order Butterworth filters respectively having cut-off frequencies $f_L = \frac{1}{4\langle \Delta t \rangle}$ and $f_H = \frac{4}{\langle \Delta t \rangle}$, which evaluated to $f_L = 120$ Hz and $f_H = 1,950$ Hz for Fig. 9a, and to $f_L = 13$ Hz and $f_H = 215$ Hz for Fig. 9b. Although the isolation of action potentials and local field potentials is often a non-trivial matter, these settings denote a

representative frequency separation deemed sufficient for the present explanatory purpose [75].

The time-series thus filtered and the associated analyses are presented in Fig. 10. While the amplitude of the high-frequency component was comparable, the low-frequency component was considerably stronger in the second case, as indicated by the root-mean-square amplitude relative to that of the unfiltered signal, which was 0.29 vs. 0.05. Accordingly, the spike-triggered average of the low-frequency component dwelt near-zero in Fig. 10a, but was approximately four times larger and had an asymmetric sinc-like appearance in Fig. 10b, prominently demonstrating the expected coupling between the two aspects of activity [76]. Also the corresponding attractor had more discernible structure in the second case, a finding which was confirmed by the fact that the permutation entropy calculated on the extrema was more distant from the surrogates compared to the first case, i.e., $h_5^{(L,E)} = 0.70$ (0.74) (Fig. 10a) vs. $h_5^{(L,E)} = 0.66$ (0.76) (Fig. 10b). A similar difference was detected for the inter-spike intervals, i.e., $h_5^{(\Delta t)} = 0.94$ (0.98) (Fig. 10a) vs. $h_5^{(\Delta t)} = 0.73$ (0.98) (Fig. 10b), and the Poincaré sections revealed a clear dissociation. For the first case, we observed a quantization into $\Delta t \approx 1$ ms within bursts and $\Delta t \approx 5$ ms during pauses, resulting in four point clouds apparently devoid of internal structure. For the second case, there was no evident
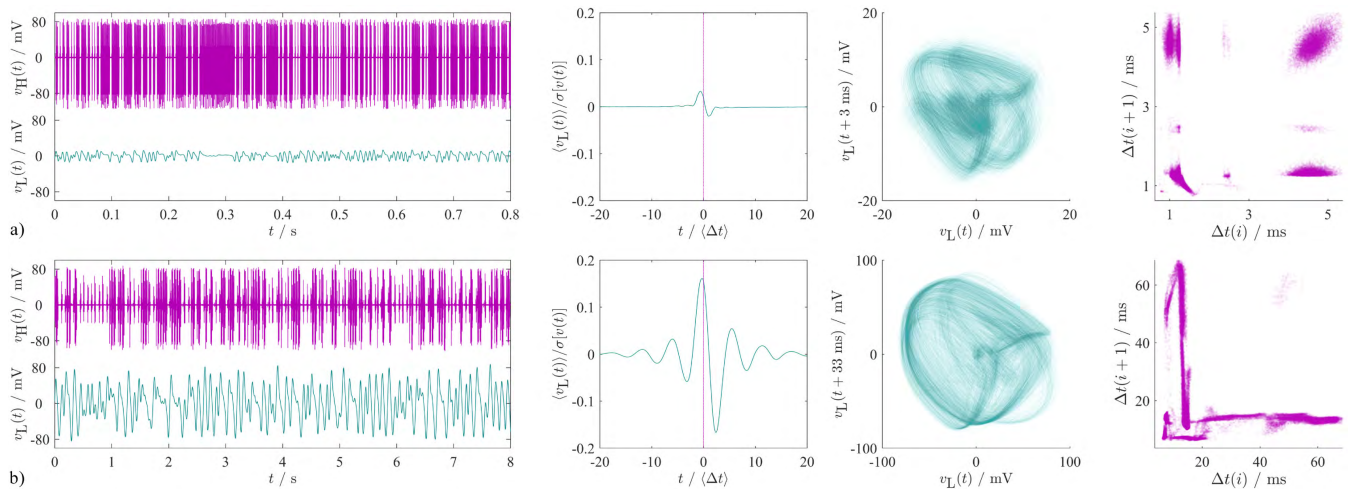
IEEE *Access*

L. Minati *et al.*: Current-Starved Cross-Coupled CMOS Inverter Rings as Versatile Generators of Chaotic and Neural-Like Dynamics

FIGURE 10. Examples of the decomposition of "neural-like" activity into an action potential-like high-frequency component ($v_H(t)$, $f > 4/\langle \Delta t \rangle$, purple) and a field potential-like low-frequency component ($v_L(t)$, $f < 1/(4\langle \Delta t \rangle)$, teal). Left to right: Frequency-filtered time-series, time-locked average of low-frequency activity with respect to the spike events (amplitude normalized to that of the raw signal $\sigma[v(t)]$, time normalized to the average inter-spike interval $\langle \Delta t \rangle$), time-lag embedded attractor of low-frequency component, Poincaré section showing successive inter-spike times. Rows a) and b) correspond to the same settings as in Fig. 9. Sign inversion applied for b).

quantization neither within nor between the bursts, resulting in a broad distribution.

Summing up, in the first case we observed the generation of spikes having binarized amplitude, with possibly a signature of criticality, however the spike timings were highly stereotyped and there were no convincing fluctuations resembling local field potentials. On the other hand, in the second case the spike timings were less stereotyped yet more predictable, and the baseline also featured local field potential-like fluctuations, however the spike amplitudes also varied, thus deviating substantially from an all-or-nothing response.

Altogether, these observations illustrate the considerable potential of the proposed circuit in generating dynamics qualitatively different from the signal features recurrently described in the previous sections. It appears remarkable that neural-like signals having diverse qualitative features could be generated purely as an emergent property, that is, without any a-priori design effort. This is reminiscent of the situation for the two-transistor spiking oscillator [13], and different with respect to the prescriptive design principles behind the circuit topologies widely used in neuromorphic computing [35]. Notably, observing these behaviors required fine-tuning the control parameters of each individual device specimen, and as such was not possible with the previous realization of this circuit, wherein current starving was not implemented, and coupling strengths could only be chosen between two levels [40]. Future simulation work should address the precise requirements for transitioning to the generation of action potential- and local field potential-like signals.

B. OSCILLATION QUENCHING

The circuit comprises three rings which, when uncoupled and supplied with identical currents, intrinsically oscillate at mismatched frequencies $\omega \propto \frac{1}{3}$, $\frac{1}{5}$ and $\frac{1}{7}$; furthermore, it is possible to fine-tune these frequencies via the control voltages V_{B3}, V_{B5} and V_{B7}, as well as to adjust the cross-coupling strengths. For these reasons, one expects that there may exist control parameter setting combinations at which the oscillators, i.e., the inverter rings, interact with each other in such a manner as to mutually suppress their activity. Oscillation quenching, first observed between pipes in church organs, is a pervasive nonlinear phenomenon which may occur as a consequence of diverse factors that, depending on system features such as the degree of mismatching, delineate two categories dubbed oscillation death and amplitude death [77]. In this scenario, given the presence of large mismatches [78], [79], as well as of a form of nonlinear coupling [80], the possible occurrence of amplitude death is predicted, wherein the system returns to a homogeneous steady state for particular parameter combinations.

Oscillation quenching is known to occur in diverse coupled nonlinear systems, including paradigmatic cases such as the Brusselator and the Stuart-Landau equation, and extending to a multitude of chemical, biological and electrical entities, including chaotic oscillators such as the Lorenz system and neural models under situations of competition [77]. Amplitude death has been reported for experimental electronic circuits such as coupled Van der Pol oscillators [81], realizations of Chua's oscillator based on operational amplifiers [82], configurations involving a delay element [83] and even coupled electronic-biological oscillators [84]. Here, no attempt is made to rigorously derive the conditions for oscillation quenching, nor, due to the experimental inaccessibility of all system variables except voltage at a chosen node, to distinguish oscillation vs. amplitude death; more simply, some observations are reported to illustrate the occurrence of this phenomenon.
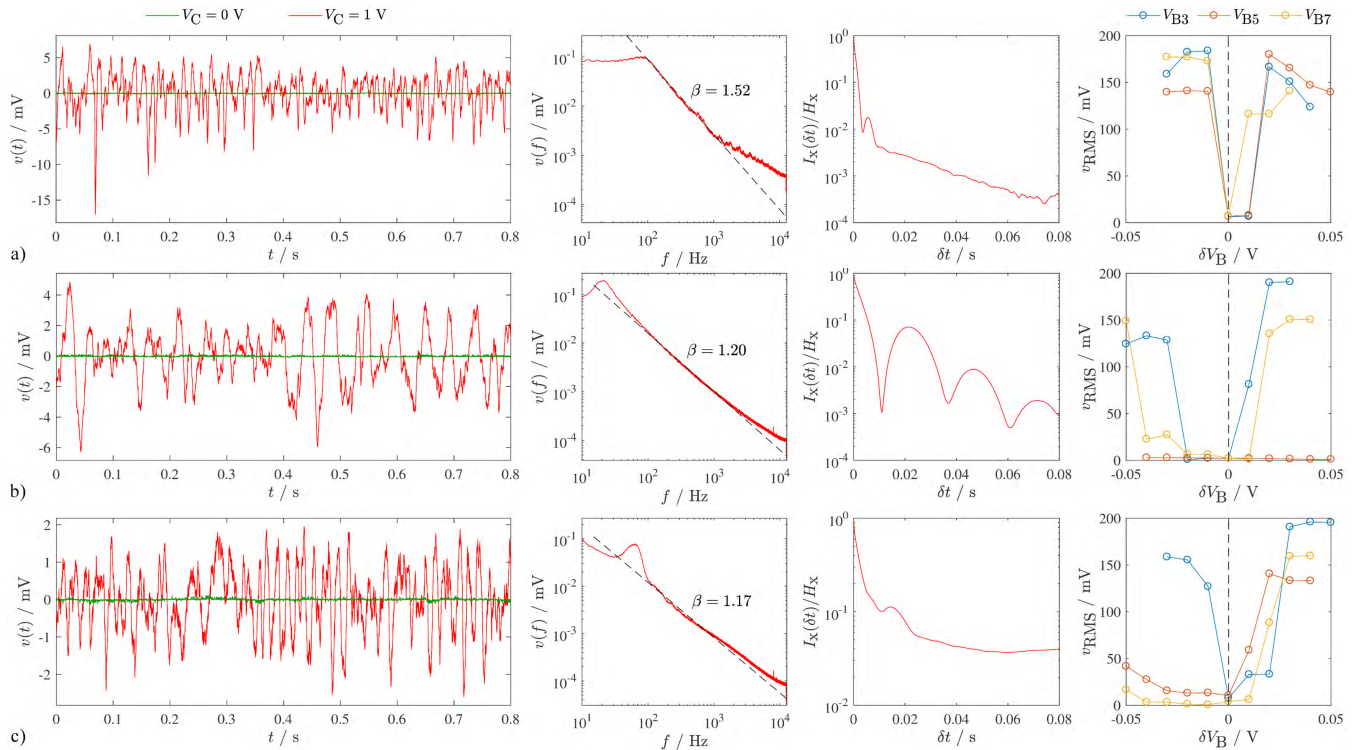
L. Minati *et al.*: Current-Starved Cross-Coupled CMOS Inverter Rings as Versatile Generators of Chaotic and Neural-Like Dynamics

IEEE Access

FIGURE 11. Examples of oscillation quenching situations. Left to right: Time-series (red: $V_C = 1$ V, green: $V_C = 0$ V), frequency spectrum (power-law with slope β fit to scaling region), time-lag normalized mutual information ($I_x(\delta t)/H_x$), root-mean-square oscillation amplitude as a function of the control voltages V_{B3}, V_{B5} and V_{B7}. a) $V_F = 1.60$ V, $V_O = 0.6$ V, $V_{B3} = 0.21$ V, $V_{B5} = 0.21$ V, $V_{B7} = 0.20$ V, $w = 0.25$ μm, $u = 1$; b) $V_F = 1.62$ V, $V_O = 0.60$ V, $V_{B3} = 0.14$ V, $V_{B5} = 0.04$ V, $V_{B7} = 0.10$ V, $w = 0.25$ μm, $u = 2$; c) $V_F = 1.62$ V, $V_O = 0.60$ V, $V_{B3} = 0.12$ V, $V_{B5} = 0.10$ V, $V_{B7} = 0.08$ V, $w = 0.25$ μm, $u = 4$. Sample rate: 25 kSa/s.

Similarly to the generation of spiking signals, oscillation quenching was experimentally found for narrow regions or isolated points, which depended on the individual tolerances of the realized devices. The time-series for three representative examples from different circuit specimens and the associated analyses are shown in Fig. 11, wherein the generation of very low-amplitude, noise-like signals of significantly greater irregularity than the deterministic chaotic oscillations is evident. The corresponding dynamical parameters are given in Table 3, and indicate that, in these cases, the root-mean-square amplitude was reduced to $\approx$ 2 mV, i.e., about 70 times lower compared to the situations of sustained oscillation. Importantly, this value was nevertheless substantially higher than the one, $\approx$ 40 μV, obtained when removing the supply voltage to the inverter rings while maintaining the output buffer active, confirming that the ring circuits themselves were amplifying the stochastic activity.

The correlation dimension and its uncertainty were considerably higher for these signals than for the recordings of sustained oscillation, with $D_2 > 5$, $\delta D_2 > 7$, and no significant difference with respect to the surrogates; the permutation entropy, which in this case was calculated via time-delay embedding, was accordingly near-unitary, i.e., $h_5^{(\tau)} \approx 1$. The frequency spectra resembled scale-free $1/f^\beta$-like distributions, with some deviations which plausibly reflected the frequency response of the circuit at the given control

parameter settings, as well as the bandwidth of the readout chain; the corresponding slope, $\beta \approx 1.2$-1.5 was in the same range established for other physical systems, notably including spontaneous brain activity [85]. The time-lag normalized mutual information, which also indexes nonlinear correlations [58], decayed in a similar manner, albeit with greater heterogeneity between the signals, and with some evidence of periodic structure in the second one. The Hurst exponent H (not to be confused with the permutation entropy h) for these signals was, respectively, 0.54 ± 0.06, 0.59 ± 0.003 and 0.64 ± 0.002, indicating mild persistence; it was always higher than in the corresponding signals acquired without applying the core supply voltage (i.e., $V_C = 0$ V, $p \leq 0.005$). These results plausibly reflect the fact that, even under oscillation quenching, the circuit possesses an intrinsic nonlinear dynamical response and, again, these measurements overlap the range $H \approx 0.5$-0.6 characterizing brain activity as visible to the electroencephalogram [86]. Sweeping the control voltages V_{B3}, V_{B5} and V_{B7} indicated that, at the available resolution, amplitude death occurred only over 2-3 points for the current starving setting of the 3-ring, even though in two cases it appeared less sensitive to the settings of the 5-ring and 7-ring.

The generation of a stochastic signal under amplitude death is not surprising, as the experimental system possesses multiple sources of diversely-colored noise, and the cascaded and reentrant response of the inverters in each ring

IEEE *Access*

L. Minati *et al.*: Current-Starved Cross-Coupled CMOS Inverter Rings as Versatile Generators of Chaotic and Neural-Like Dynamics

can yield a high gain. Noise amplification in the vicinity of transition to amplitude death has been previously reported for instance in thermoacoustic oscillators [87], and represents an instance of a more general class of instabilities in nonlinear systems revealed by the administration of external noise [88]. On the other hand, it has been shown that amplitude death can also be in itself inducted by sufficiently strong intrinsic noise [89]. Since oscillation quenching is arguably as universal a phenomenon as mechanisms of pattern formation via symmetry breaking such as cluster synchronization [77], and its occurrence is of interest to specific applications such as in neurostimulation [84], the present observations further corroborate the generality of the behavior of the proposed circuit. As noted for the generation of spiking signals, oscillation quenching required fine-tuning the control parameters of each individual device specimen, and was thus inherently inaccessible in the previous realization of this circuit where such adjustments could not be performed [40].

V. CONCLUDING REMARKS AND FUTURE WORK

We have illustrated the design and experimental characterization of a pure-CMOS chaotic oscillator whose architecture hinges around the capability of cross-coupled inverter rings to generate rich nonlinear dynamics. In this circuit, the onset of chaos is enabled by the interactions between the rings having mismatched lengths and consequently natural oscillation frequencies not related by trivial ratios.

In particular, the introduction of current starving into the preexisting design of this circuit was shown to add fundamentally important control parameters, which could determine the qualitative features of the dynamics as well as continuously tune the oscillation frequency over a broad range while retaining chaoticity. Accordingly, as a function of these parameters, chaotic attractors featuring different topological characteristics were consistently obtained in the fabricated devices. Notably, the same parameters also controlled the appearance and disappearance of spiking behaviors, with quantized amplitudes or slow field potential-like fluctuations, and of oscillation-quenching states characterized by primarily stochastic activity. The qualitative features of the generated signals were reminiscent of neurophysiological recordings acquired, respectively, at the micro- and mesoscopic scales, and at the macroscale. On the other hand, the possibility of straightforwardly shifting the frequency spectrum is relevant to applications requiring the generation of dynamics unfolding on a specific time scale, such as found in random number generation, chaotic modulation schemes, chaos-based control applications and wireless communication. Notably, the main qualitative features of chaos generation across different frequencies were captured in close agreement by the simulations using simplified numerical models, by the SPICE simulations and by the experiments; at the same time, due to the increasing complexity owing to the type of nonlinearity, the tolerances and nonidealities, the richness of

the observed behaviors gradually increased over these three scenarios.

The design encompassing an architecture avoiding entirely the need for reactive and resistive components makes the proposed circuit particularly efficient in terms of area occupancy, a feature which is of central importance in applications such as the experimental realization of large-scale coupled-oscillator networks. Future work should harvest the generative potential of this circuit in realizing such networks, and additionally address the optimization of the relevant circuit features (e.g., transistor geometries) towards the specific dynamics of interest in each application: for instance, the generation of spiking signals or the maximization of dynamics reproducibility across device specimens subject to different manufacturing tolerances. Furthermore, ongoing research will address the value of this circuit as a building block for realizing distributed sensing networks, wherein individual nodes are wirelessly coupled to their neighbors and the non-linear system dynamics lead to emergent phenomena supporting the efficient detection of changes of interest, maximizing sensitivity while minimizing bandwidth requirements: for instance, changes in the strain of a structure or in the chemical composition of a soil could drive phase transitions between chaotic and periodic dynamics through collective behaviors expressed at the network level. Towards this end, it will be necessary to port the design to even smaller geometries, further reducing the power draw while increasing frequency, and to develop effective approaches for connecting, directly or indirectly, sensing elements to the oscillating rings.

REFERENCES

[1] G. Kaddoum, "Wireless chaos-based communication systems: A comprehensive survey," *IEEE Access*, vol. 4, pp. 2621–2648, May 2016.

[2] J. D. J. Golic, "New methods for digital generation and postprocessing of random data," *IEEE Trans. Comput.*, vol. 55, no. 10, pp. 1217–1229, Oct. 2006.

[3] A. Buscarino, L. Fortuna, M. Frasca, and G. Muscato, "Chaos does help motion control," *Int. J. Bifurcation Chaos*, vol. 17, no. 10, pp. 3577–3581, 2007.

[4] P. Arena, S. de Fiore, L. Fortuna, M. Frasca, L. Patané, and G. Vagliasindi, "Reactive navigation through multiscroll systems: From theory to real-time implementation," *Auton. Robots*, vol. 25, nos. 1–2, pp. 123–146, Dec. 2007.

[5] L. Fortuna, M. Frasca, and A. Rizzo, "Chaotic pulse position modulation to improve the efficiency of sonar sensors," *IEEE Trans. Instrum. Meas.*, vol. 52, no. 6, pp. 1809–1814, Dec. 2003.

[6] Z. Liu, X. Zhu, W. Hu, and F. Jiang, "Principles of chaotic signal radar," *Int. J. Bifurc. Chaos*, vol. 17, no. 5, pp. 1735–1739, May 2007.

[7] S. Barbarossa and F. Celano, "Self-organizing sensor networks designed as a population of mutually coupled oscillators," in *Proc. IEEE 6th Workshop Signal Process. Adv. Wireless Commun.*, Jun. 2005, pp. 475–479.

[8] Y. Zong, X. Dai, Z. Gao, R. Binns, and K. Busawon, "Simulation and evaluation of pulse-coupled oscillators in wireless sensor networks," *Syst. Sci. Control Eng.*, vol. 6, no. 1, pp. 337–349, Jan. 2018.

L. Minati *et al.*: Current-Starved Cross-Coupled CMOS Inverter Rings as Versatile Generators of Chaotic and Neural-Like Dynamics

IEEE*Access*

[9] A. Díaz-Guilera, A. Arenas, L. Pietro, E. Yoneki, J. Crowcroft, and D. C. Verma, "Phase patterns of coupled oscillators with application to wireless communication," in *Bio-Inspired Computing and Communication* (Lecture Notes in Computing Science), vol. 5151. Berlin, Germany: Springer-Verlag, 2008, pp. 184–191.

[10] A. S. Elwakil and M. P. Kennedy, "A low-voltage, low-power, chaotic oscillator, derived from a relaxation oscillator," *Microelectron. J.*, vol. 31, no. 6, pp. 459–468, Jun. 2000.

[11] N. F. Rulkov and A. R. Volkovskii, "Generation of broad-band chaos using blocking oscillator," *IEEE Trans. Circuits Syst. I, Fundam. Theory Appl.*, vol. 48, no. 6, pp. 673–679, Jun. 2001.

[12] E. Lindberg, K. Murali, and A. Tamasevicius, "The smallest transistor-based nonautonomous chaotic circuit," *IEEE Trans. Circuits Syst. II, Express Briefs*, vol. 52, no. 10, pp. 661–664, Oct. 2005.

[13] L. Minati, M. Frasca, P. Oświęcimka, L. Faes, and S. Drożdż, "Atypical transistor-based chaotic oscillators: Design, realization, and diversity," *Chaos*, vol. 27, no. 7, Jul. 2017, Art. no. 073113.

[14] J. C. Sprott, "A new chaotic jerk circuit," *IEEE Trans. Circuits Syst. II, Express Briefs*, vol. 58, no. 4, pp. 240–243, Apr. 2011.

[15] A. Buscarino, L. Fortuna, M. Frasca, and G. Sciuto, "Design of time-delay chaotic electronic circuits" *IEEE Trans. Circuits Syst. I, Reg. Papers*, vol. 58, no. 8, pp. 1888–1896, Feb. 2011.

[16] J. M. Cruz and L. O. Chua, "An IC chip of Chua's circuit," *IEEE Trans. Circuits Syst. II, Analog Digit. Signal Process.*, vol. 40, no. 10, pp. 614–625, Oct. 1993.

[17] A. Rodríguez-Vázquez, and M. Delgado-Restituto, "CMOS design of chaotic oscillators using state variables: A monolithic Chua's circuit," *IEEE Trans. Circuits Syst. II, Analog Digit. Signal Process.*, vol. 40, no. 10, pp. 596–613, Oct. 1993.

[18] P. Arena, S. Castorina, L. Fortuna, M. Frasca, and A. Rizzo, "An integrated Chua's cell for the implementation of a Chua's array," *Int. J. Bifurc. Chaos*, vol. 14, no. 1, pp. 93–105, Jan. 2004.

[19] T. Asai, T. Kamiya, T. Hirose, and Y. Amemiya, "A subthreshold analog MOS circuit for Lotka—Volterra chaotic oscillator," *Int. J. Bifurcation Chaos*, vol. 16, no. 1, pp. 207–212, 2006.

[20] J. L. Rosselló, V. Canals, I. de Paul, S. Bota, and A. Morro, "A simple CMOS chaotic integrated circuit," *IEICE Electron. Express*, vol. 5, no. 24, pp. 1042–1048, May 2008.

[21] J. M. Muñoz-Pacheco, I. E. Flores-Tiro, and R. Trejo-Guerra, "Experimental synchronization of two integrated multi-scroll chaotic oscillators," *J. Appl. Res. Technol.*, vol. 12, no. 3, pp. 459–470, Jun. 2014.

[22] V. Tavas, A. S. Demirkol, S. Ozoguz, A. Zeki, and A. Toker, "An ADC based random bit generator based on a double scroll chaotic circuit," *J. Circuits, Syst., Comput.*, vol. 19, no. 7, pp. 1621–1639, 2010.

[23] V. Tavas, A. S. Demirkol, S. Ozoguz, A. Zeki, and A. Toker, "Integrated cross-coupled chaos oscillator applied to random number generation," *IET Circuits, Devices Syst.*, vol. 3, no. 1, pp. 1–11, Feb. 2009.

[24] V. D. Juncu, M. Rafiei-Naeini, and P. Dudek, "Integrated circuit implementation of a compact discrete-time chaos generator," *Analog Integr. Circuits Signal Process.*, vol. 46, no. 3, pp. 275–280, Mar. 2006.

[25] B. Kia, K. Mobley, and W. L. Ditto, "An integrated circuit design for a dynamics-based reconfigurable logic block," *IEEE Trans. Circuits Syst. II, Exp. Briefs*, vol. 64, no. 6, pp. 715–719, May 2017. doi: 10.1109/TCSII.2016.2611442.

[26] R. Trejo-Guerra, E. Tlelo-Cuautle, M. Jiménez-Fuentes, J. Muñoz-Pacheco, and C. Sánchez-López, "Multiscroll floating gate-based integrated chaotic oscillator," *Int. J. Circuit Theory Appl.*, vol. 41, no. 8, pp. 831–843, Dec. 2011.

[27] J. Nunez, E. Tlelo, C. Ramirez, and J. Jimenez, "CCII+ based on QFG-MOS for implementing chua s chaotic oscillator," *IEEE Latin Amer. Trans.*, vol. 13, no. 9, pp. 2865–2870, Dec. 2015.

[28] V. H. Carbajal-Gomez, E. Tlelo-Cuautle, J. M. Muñoz-Pacheco, L. G. de la Fraga, C. Sanchez-Lopez, and F. V. Fernandez-Fernandez, "Optimization and CMOS design of chaotic oscillators robust to PVT variations: INVITED," *Integration*, to be published.

[29] R. Trejo-Guerra, E. Tlelo-Cuautle, V. H. Cabajal-Gómez, and G. Rodriguez-Gómez, "A survey on the integrated design of chaotic oscillators," *Appl. Math. Comput.*, vol. 219, no. 10, pp. 5113–5122, Jan. 2013. doi: 10.1016/j.amc.2012.11.021.

[30] F. Yu, P. Li, K. Gu, and B. Yin, "Research progress of multi-scroll chaotic oscillators based on current-mode devices," *Optik*, vol. 127, no. 3, pp. 5486–5490, 2016.

[31] C. R. Williams, F. Sorrentino, T. E. Murphy, and R. Roy, "Synchronization states and multistability in a ring of periodic oscillators: Experimentally variable coupling delays," *Chaos*, vol. 23, no. 4, Oct. 2013, Art. no. 043117.

[32] L. Minati, "Experimental synchronization of chaos in a large ring of mutually coupled single-transistor oscillators: Phase, amplitude, and clustering effects," *Chaos, Interdiscipl. J. Nonlinear Sci.*, vol. 24, no. 4, Dec. 2014, Art. no. 043108.

[33] S. Boccaletti *et al.*, *Synchronization: From Coupled Systems to Complex Networks*. Cambridge, U.K.: Cambridge Univ. Press, 2018.

[34] C. Mead, *Analog VLSI and Neural Systems*. Boston MA, USA: Addison-Wesley, (1989).

[35] G. Indiveri *et al.*, "Neuromorphic silicon neuron circuits," *Frontiers Neurosci.*, vol. 5, p. 73, May 2011.

[36] B. Sunar, W. J. Martin, and D. R. Stinson, "A provably secure true random number generator with built-in tolerance to active attacks," *IEEE Trans. Comput.*, vol. 56, no. 1, pp. 109–119, Jan. 2007.

[37] Y. Hosokawa and Y. Nishio, "Simple chaotic circuit using CMOS ring oscillators," *Int. J. Bifurc. Chaos*, vol. 14, no. 7, pp. 2513–2524, Jul. 2004.

[38] Y. Tanaka, J. Yoshimura, C. Simon, J. R. Cooley, and K. Tainaka, "Allee effect in the selection for prime-numbered cycles in periodical cicadas," *Proc. Nat. Acad. Sci.*, vol. 106, no. 22, pp. 8975–8979, Jun. 2009.

[39] H. Ito *et al.*, "Evolution of periodicity in periodical cicadas," *Sci. Rep.*, vol. 5, Sep. 2015, Art. no. 14094.

[40] L. Minati, "Experimental implementation of networked chaotic oscillators based on cross-coupled inverter rings in a CMOS integrated circuit," *J. Circuits, Syst. Comput.*, vol. 24, no. 9, Aug. 2015, Art. no. 1550144.

[41] L. F. Shampine and M. W. Reichelt, "The MATLAB ODE suite," *SIAM J. Sci. Comput.*, vol. 18, no. 1, pp. 1–22, 1997.

[42] J. M. Grey and J. W. Gordon, "Perceptual effects of spectral modifications on musical timbres," *J. Acoust. Soc. Amer.*, vol. 63, no. 5, p. 1493, May 1978.

[43] H. Kantz and T. Schreiber, *Nonlinear Time Series Analysis*. Cambridge, U.K.: Cambridge Univ. Press, 1997.

[44] R. Hegger, H. Kantz, and T. Schreiber, "Practical implementation of nonlinear time series methods: The TISEAN package," *Chaos*, vol. 9, p. 413, May 1999.

[45] P. Grassberger and I. Procaccia, "Measuring the strangeness of strange attractors," *Phys. D, Nonlinear Phenomena*, vol. 9, no. 1, pp. 189–208, Oct. 1983.

[46] H. Kantz, "A robust method to estimate the maximal Lyapunov exponent of a time series," *Phys. Lett. A*, vol. 185, no. 1, pp. 77–87, Jan. 1994.

[47] J. D. Johnston, "Transform coding of audio signals using perceptual noise criteria," *IEEE J. Sel. Areas Commun.*, vol. 6, no. 2, pp. 314–323, Feb. 1988.

[48] S. Boccaletti, J. Kurths, G. Osipov, D. L. Valladares, and C. S. Zhou, "The synchronization of chaotic systems," *Phys. Rep.*, vol. 366, nos. 1–2, pp. 1–101, 2002.

[49] J. R. Dormand and P. J. Prince, "A family of embedded Runge-Kutta formulae," *J. Comput. Appl. Math.*, vol. 6, no. 1, pp. 19–26, 1980.

[50] G. Benettin, L. Galgani, A. Giorgilli, and J. M. Strelcyn, "Lyapunov characteristic exponents for smooth dynamical systems and for hamiltonian systems; A method for computing all of them. Part 1: Theory," *Meccanica*, vol. 15, no. 1, pp. 9–20, Mar. 1980.

[51] G. Benettin, L. Galgani, A. Giorgilli, and J. Strelcyn, "Lyapunov characteristic exponents for smooth dynamical systems and for hamiltonian systems; A method for computing all of them. Part 2: Numerical application," *Meccanica*, vol. 15, no. 1, pp. 21–30, Mar. 1980.

[52] C. Skokos, "The Lyapunov Characteristic Exponents and Their Computation," *Lect Notes Phys.*, vol. 790, pp. 63–135, Nov. 2010.

[53] M. Franchi and L. Ricci, "Statistical properties of the maximum Lyapunov exponent calculated via the divergence rate method," *Phys. Rev. E, Stat. Phys. Plasmas Fluids Relat. Interdiscip. Top.*, vol. 90, no. 6, Dec. 2014, Art. no. 062920.

[54] J. L. Kaplan and J. A. Yorke, "Chaotic behavior of multidimensional difference equations," in *Functional Differential Equations and Approximation of Fixed Points*. Heidelberg, Germany: Springer, 1979, pp. 204–227.

[55] B. Razavi, *Design of Analog CMOS Integrated Circuits*. New York, NY, USA: McGraw-Hill, 2000.

[56] (2018). *Predictive Technology Model (PTM) for Bulk CMOS 180 nm*. [Online]. Available: http://ptm.asu.edu/modelcard/180nm_bulk.txt

[57] (2019). *Publicly Available Data*. [Online]. Available: http://www.lminati.it/listing/2019/a/

IEEE *Access*

L. Minati *et al.*: Current-Starved Cross-Coupled CMOS Inverter Rings as Versatile Generators of Chaotic and Neural-Like Dynamics

[58] A. M. Fraser and H. L. Swinney, ''Independent coordinates for strange attractors from mutual information,'' *Phys. Rev. A, Gen. Phys.*, vol. 33, no. 2, pp. 1134–1140, Feb. 1986.

[59] L. Minati, ''Across neurons and silicon: Some experiments regarding the pervasiveness of nonlinear phenomena,'' *Acta Phys. Pol. B*, vol. 49, no. 12, pp. 2029–2094, Dec. 2018.

[60] A. Buscarino, L. Fortuna, M. Frasca, and G. Sciuto, *A Concise Guide to Chaotic Electronic Circuits* Berlin, Germany: Springer, 2014.

[61] T. Schreiber and A. Schmitz, ''Improved surrogate data for nonlinearity tests,'' *Phys. Rev. Lett.*, vol. 77, no. 4, pp. 635–638, 1996.

[62] C. Bandt and B. Pompe, ''Permutation entropy: A natural complexity measure for time series,'' *Phys. Rev. Lett.*, vol. 88, no. 17, p. 174102, 2002.

[63] M. Riedl, A. Müller, and N. Wessel, ''Practical considerations of permutation entropy,'' *Eur. Phys. J. Special Topics*, vol. 222, no. 2, pp. 249–262, Jun. 2013.

[64] E. Ott, *Chaos in Dynamical Systems* Cambridge, U.K.: Cambridge Univ. Press, 2002.

[65] M. P. Kennedy, ''Chaos in the Colpitts oscillator,'' *IEEE Trans. Circuits Syst. I, Fundam. Theory Appl.*, vol. 41, no. 11, pp. 771–774, Nov. 1994. doi: 10.1109/81.331536.

[66] B. Davis, J. Jovicich, V. Iacovella, and U. Hasson, ''Functional and developmental significance of amplitude variance asymmetry in the BOLD resting-state signal,'' *Cerebrel Cortex*, vol. 24, no. 5, pp. 1332–1350, May 2014.

[67] M. I. Rabinovich, P. Varona, A. I. Selverston, and H. D. I. Abarbanel, ''Dynamical principles in neuroscience,'' *Rev. Mod. Phys.*, vol. 78, pp. 1213–1265, Nov. 2006.

[68] L. Minati, ''Experimental dynamical characterization of five autonomous chaotic oscillators with tunable series resistance,'' *Chaos*, vol. 24, Jul. 2014, Art. no. 033110.

[69] I. T. Georgiou, I. T. Schwartz, E. Emaci, and A. Vakakis, ''Interaction between slow and fast oscillations in an infinite degree-of-freedom linear system coupled to a nonlinear subsystem: Theory and experiment,'' *J. Appl. Mech.*, vol. 66, no. 2, pp. 448–459, Oct. 1999.

[70] W. H. Matthaeus *et al.*, ''Intermittency, nonlinear dynamics and dissipation in the solar wind and astrophysical plasmas'' *Philos. Trans. Roy. Soc. A, Math., Phys. Eng. Sci.*, vol. 373, no. 2041, May 2015, Art. no. 20140154.

[71] M. A. Buice and J. D. Cowan, ''Statistical mechanics of the neocortex,'' *Prog. Biophys. Mol. Biol.*, vol. 99, no. 2, pp. 53–86, Mar. 2009.

[72] L. Minati, A. de Candia, and S. Scarpetta, ''Critical phenomena at a first-order phase transition in a lattice of glow lamps: Experimental findings and analogy to neural activity,'' *Chaos*, vol. 26, Jun. 2016, Art. no. 073103.

[73] J. M. Beggs and D. Plenz, ''Neuronal avalanches in neocortical circuits,'' *J. Neurosci.*, vol. 23, no. 35, pp. 11167–11177, Dec. 2003.

[74] C. Tetzlaff, S. Okujeni, U. Egert, F. Wórgötter, and M. Butz, ''Self-organized criticality in developing neuronal networks,'' *PLoS Comput. Biol.*, vol. 6, no. 12, Dec. 2010, Art. no. e1001013.

[75] S. Waldert, R. N. Lemon, and A. Kraskov, ''Influence of spiking activity on cortical local field potentials,'' *J Physiol.*, vol. 591, no. 21, pp. 5291–5303, Nov. 2013.

[76] B. Telećzuk, S. N, Baker, R. Kempter, and G. Curio, ''Correlates of a single cortical action potential in the epidural EEG,'' *NeuroImage*, vol. 109, pp. 357–367, Apr. 2015.

[77] A. Koseska, E. Volkov, and J. Kurths, ''Oscillation quenching mechanisms: Amplitude vs. oscillation death,'' *Phys. Rep.*, vol. 531, no. 4, pp. 173–199, Oct. 2013.

[78] R. E. Mirollo and S. H. Strogatz, ''Amplitude death in an array of limit-cycle oscillators,'' *J. Stat. Phys.*, vol. 60, no. 1, pp. 245–262, Jul. 1990.

[79] B. Ermentrout, ''Oscillator death in populations of 'all to all' coupled nonlinear oscillators,'' *Phys. D, Nonlinear Phenomena*, vol. 41, no. 2, pp. 219–231, Mar. 1990.

[80] A. Prasad, M. Dhamala, B. M. Adhikari, and R. Ramaswamy, ''Amplitude death in nonlinear oscillators with nonlinear coupling,'' *Phys. Rev. E, Stat. Phys. Plasmas Fluids Relat. Interdiscip. Top.*, vol. 81, p. 027201, Feb. 2010.

[81] T. Banerjee and D. Ghosh, ''Experimental observation of a transition from amplitude to oscillation death in coupled oscillators,'' *Phys. Rev. E, Stat. Phys. Plasmas Fluids Relat. Interdiscip. Top.*, vol. 89, Jun. 2014, Art. no. 062902.

[82] K. Suresh, M. D. Shrimali, A. Prasad, and K. Thamilmaran, ''Experimental evidence for amplitude death induced by a time-varying interaction,'' *Phys. Lett. A*, vol. 378, no. 38, pp. 2845–2850, Aug. 2014.

[83] K. Konishi, K. Senda, and H. Kokam, ''Amplitude death in time-delay nonlinear oscillators coupled by diffusive connections,'' *Phys. Rev. E, Stat. Phys. Plasmas Fluids Relat. Interdiscip. Top.*, vol. 78, Nov. 2008, Art. no. 056216.

[84] I. Ozden, S. Venkataramani, M. A. Long, B. W. Connors, and A. V. Nurmikko, ''Strong coupling of nonlinear electronic and biological oscillators: Reaching the 'amplitude death,' regime,'' *Phys. Rev. Lett.*, vol. 93, no. 15, Oct. 2004, Art. no. 158102.

[85] B. J. He, ''Scale-free brain activity: Past, present, and future,'' *Trends Cogn. Sci.*, vol. 18, no. 9, pp. 480–487, Apr. 2014.

[86] D. A. Blythe, S. Haufe, and K. R. Müller, and V. V. Nikulin, ''The effect of linear mixing in the EEG on Hurst exponent estimation,'' *NeuroImage*, vol. 99, pp. 87–377, Oct. 2014.

[87] N. Thomas, S. Mondal, S. A. Pawar, and R. I. Sujith, ''Effect of noise amplification during the transition to amplitude death in coupled thermoacoustic oscillators,'' *Chaos*, vol. 28, Sep. 2018, Art. no. 093116.

[88] K. Wiesenfeld, ''Noisy precursors of nonlinear instabilities,'' *J. Stat. Phys*, vol. 38, no. 5, pp. 1071–1097, Mar. 1985.

[89] O. Díaz-Hernández *et al.*, ''Amplitude death induced by intrinsic noise in a system of three coupled stochastic brusselators,'' *J. Comput. Nonlinear Dynam.*, vol. 14, no. 4, Feb. 2019, Art. no. 041004.

LUDOVICO MINATI (AM'00–M'04–SM'13) received the B.S. degree in information technology and computing and the M.S. degree in science from The Open University, Milton Keynes, U.K., in 2004 and 2006, respectively, the M.S. degree in applied cognitive neuroscience from the University of Westminster, London, U.K., in 2008, the B.S. degree in physical science and the M.S. degree in medical physics from The Open University, in 2009, the Ph.D. degree in neuroscience from the Brighton and Sussex Medical School, U.K., in 2012, and the D.Sc. (doktor habilitowany) degree in physics from the Institute of Nuclear Physics, Polish Academy of Sciences, Kraków, Poland, in 2017.

He has held research and consulting roles across private companies and public institutions, including the Carlo Besta Neurological Institute, Milan, Italy; and the Brighton and Sussex Medical School, U.K. He has authored over 110 articles and five patents. He is currently a specially appointed Associate Professor with the Institute of Innovative Research, Tokyo Institute of Technology, Japan; a Visiting Professor with the Complex Systems Theory Department, Institute of Nuclear Physics-Polish Academy of Sciences; a Guest Fellow of the Center for Mind/Brain Sciences, University of Trento, Italy; and a Freelance R&D Consultant. His research interests include non-linear dynamical systems, chaotic oscillators, reconfigurable analog and digital computing, functional magnetic resonance imaging, advanced techniques for bio-signal analysis, brain machine/computer interfaces, and robotics.

Dr. Minati is also a Chartered Engineer and a member of the Institution of Engineering and Technology, U.K., a Chartered Physicist and a member of the Institute of Physics, London, U.K., and a Chartered Scientist and a member of the Institute of Physics and Engineering in Medicine, York, U.K. He is also a member of the Institute of Electronics, Information, and Communication Engineers (IEICE), and the Japan Neuroscience Society.

L. Minati *et al.*: Current-Starved Cross-Coupled CMOS Inverter Rings as Versatile Generators of Chaotic and Neural-Like Dynamics

IEEE *Access*

MATTIA FRASCA (M'00–SM'09) received the degree in electronics engineering and the Ph.D. degree in electronics and automation engineering from the University of Catania, Italy, in 2000 and 2003, respectively, where he is currently an Associate Professor and teaches process control and systems theory.

His scientific interests include nonlinear systems and chaos, complex networks, and bio-inspired robotics. He has authored or coauthored six books and over 250 papers on refereed international journals and proceedings, and is a coauthor of two international patents.

Dr. Frasca is a member of the Board of the Italian Society for Chaos and Complexity. He was one of the organizers of the 10th Experimental Chaos Conference, the Co-Chair of the 4th International Conference on Physics and Control, and the Chair of the European Conference on Circuit Theory and Design 2017. He has also served as an Associate Editor for the IEEE TRANSACTIONS ON CIRCUITS AND SYSTEMS I, from 2012 to 2015. He is also an Associate Editor of the *International Journal of Bifurcation and Chaos*, and the Editor of the *Chaos, Solitons & Fractals* journal.

NATSUE YOSHIMURA received the M.S. degree from the Tokyo Medical and Dental University, Japan, in 2006, and the Ph.D. degree from The University of Electro-communications, Japan, in 2009.

She was a Postdoctoral Researcher with the Tokyo Institute of Technology, from 2009 to 2010, and became an Assistant Professor. She has been an Associate Professor with the Institute of Innovative Research, Tokyo Institute of Technology, since 2015. She is currently a Visiting Researcher with the Integrative Brain Imaging Center, National Center of Neurology and Psychiatry. Her research interests include brain machine/computer interfaces; brain activity information decoding relating to motor control, speech, and emotion using noninvasive brain activity recording methods, such as electroencephalography; and functional magnetic resonance imaging. She is a member of the Society for Neuroscience, the Japan Neuroscience Society, and the Japanese Society for Medical and Biological Engineering.

LEONARDO RICCI (M'18) received the M.S. degree in physics from the University of Pisa, Pisa, Italy, in 1990, and the Ph.D. degree in physics from the Ludwig-Maximilian Universitaĺt, Munich, Germany, in 1994. From 1990 to 1994, he was with T. W. Hänsch's Group, Munich, Germany. In 1995, he moved to the Department of Physics, University of Trento, Trento, Italy, where he is currently an Adjunct Professor. His research interests mainly concern the investigation of the role of noise in brain function, nonlinear dynamics, and the development of nonlinear techniques for time series analysis.

PAWEŁ OŚWIĘCIMKA received the M.S. degree in physics from the AGH University of Science and Technology, Krakow, Poland, in 2001, and the Ph.D. and D.Sc. degrees in physics from the Institute of Nuclear Physics, Polish Academy of Sciences, Kraków, Poland, in 2005 and 2015, respectively.

Since 2016, he has been an Associate Professor with the Department of Theory of Complex Systems, Institute of Nuclear Physics, Polish Academy of Sciences. He is also a Lecturer with the Faculty of Physics, Mathematics and Computer Science, University of Technology, Kraków, Poland. His current research interests include interdisciplinary research in natural and social complex systems by means of advanced methods of time series analysis, with the particular emphasis on multifractal analysis, complex network analysis, and modelling of multiscaling processes. He is a Fellow of the Commission of Complex Systems, Polish Academy of Arts and Sciences (PAU), Kraków.

YASUHARU KOIKE received the B.S., M.S., and Ph.D. degrees in engineering from the Tokyo Institute of Technology, Tokyo, Japan, in 1987, 1989, and 1996, respectively.

From 1989 to 1998, he was with Toyota Motor Corporation. From 1991 to 1994, he was transferred to the Advanced Tele-communications Research Human Information Processing Laboratories, Kyoto, Japan. In 1998, he moved to the Precision and Intelligence Laboratory, Tokyo Institute of Technology, Tokyo, Japan, where he is currently a Professor with the Institute of Innovative Research. He was a Researcher of the Precursory Research for Embryonic Science and Technology, Japan Science and Technology Corporation, from 2000 to 2004, and of CREST, JST, from 2004 to 2014. His research interests include human motor control theory, human interface, and brain–machine interface and their applications.

Dr. Koike is a member of the Society for Neuroscience, the Institute of Electronics, Information and Communication Engineers (IEICE), the Virtual Reality Society of Japan, and the Japan Neuroscience Society.

KAZUYA MASU received the B.E., M.E., and Ph.D. degrees in electronics engineering from the Tokyo Institute of Technology, Tokyo, Japan, in 1977, 1979, and 1982, respectively.

He was with the Research Institute of Electrical Communication, Tohoku University, Sendai, Japan, from 1982 to 2000. In 2000, he became a Professor with the Precision and Intelligence Laboratory, Tokyo Institute of Technology, Yokohama, Japan. He has served as the Director-General of the Institute of Innovative Research, Tokyo Institute of Technology. Since 2018, he has been serving as the President of the Tokyo Institute of Technology. He was a Visiting Professor with the Georgia Institute of Technology, in 2002 and 2005, respectively. His current interests are RF CMOS circuit technology for the IoT, and ultra-high sensitive CMOS-MEMS inertia sensor and its application in early diagnosis of intractable neurological diseases.

Dr. Masu is a Fellow of the JSAP, the IEEJ, and the IEICE. He received the IEICE (Institute of Electronics, Information and Communication Engineers) Electronics Society Award, in 2004; the IEICE Achievement Award, in 2013; and the IEEJ (Institute of Electrical Engineers of Japan) Outstanding Achievement Award, in 2014. He has served as the Vice President of the Japan Society of Applied Physics (JSAP) (2014–2015), and the President of the Japan Institute of Electronics Packaging (JIEP) (2017–2019). In 2014, he has served as the Organizing Committee Chair of the International Conference of Solid State Devices and Materials (SSDM2014).

HIROYUKI ITO (S'03–M'04) received the B.E. degree from the Department of Electronics and Mechanical Engineering, Chiba University, Chiba, Japan, in 2002, and the M.E. and Ph.D. degrees from the Department of Advanced Applied Electronics, Tokyo Institute of Technology, Yokohama, Japan, in 2004 and 2006, respectively.

From 2004 to 2007, he was a Research Fellow of the Japan Society for the Promotion of Science. He was a temporary Visiting Researcher and a Visiting Professor with the Communications Technology Laboratory, Intel Corporation, Hillsboro, OR, USA, in 2006 and 2007, respectively. He was an Assistant Professor with the Precision and Intelligence Laboratory, Tokyo Institute of Technology, Yokohama, Japan, from 2007 to 2013. From 2008 to 2010, he was with the Fujitsu Laboratories Ltd., Yokohama, Japan, where he developed RF CMOS transceiver and digital calibration techniques for mobile-WiMAX application. From 2013 to 2015, he was an Associate Professor with the Precision and Intelligence Laboratory, Tokyo Institute of Technology, Yokohama, where he has been an Associate Professor with the Institute of Innovative Research, since 2016. His research interests include analog, RF, and mixed-signal circuit design for the IoT and their application. He is a member of the IEEE Solid-State Circuits Society, the Institute of Electronics, Information and Communication Engineers (IEICE), and the Japan Society of Applied Physics (JSAP).

• • •